Three-dimensional numerical modeling of thermal regime and slab dehydration beneath Kanto and Tohoku, Japan

Ji, Yingfeng
Yoshioka, Shoichi
Manea, Vlad Constantin
Manea, Marina
Matsumoto, Takumi

(Citation)
Journal of Geophysical Research: Solid,122(1):332-353

(Issue Date)
2017-01

(Resource Type)
journal article

(Version)
Version of Record

(URL)
https://hdl.handle.net/20.500.14094/90005032

AGU PUBLICATIONS

JGR

Journal of Geophysical Research: Solid Earth

RESEARCH ARTICLE
10.1002/2016JB013230

Key Points:
- 3-D thermal model for double subduction
- Slab thermal regime and water content distribution beneath Kanto and Tohoku
- The slab dehydration corresponding with with seismicity distribution beneath Kanto and Tohoku

Correspondence to:
Y. Ji,
jiyf@people.kobe-u.ac.jp

Citation:
Ji, Y., S. Yoshioka, V. C. Manea, M. Manea, and T. Matsumoto (2017), Three-dimensional numerical modeling of thermal regime and slab dehydration beneath Kanto and Tohoku, Japan, *J. Geophys. Res. Solid Earth*, *122*, 332–353, doi:10.1002/2016JB013230.

Received 2 JUN 2016
Accepted 11 DEC 2016
Accepted article online 14 DEC 2016
Published online 5 JAN 2017

Three-dimensional numerical modeling of thermal regime and slab dehydration beneath Kanto and Tohoku, Japan

Yingfeng Ji[1], Shoichi Yoshioka[1,2], Vlad Constantin Manea[3,4], Marina Manea[3,4], and Takumi Matsumoto[5]

[1]Research Center for Urban Safety and Security, Kobe University, Kobe, Japan, [2]Department of Planetology, Graduate School of Science, Kobe University, Kobe, Japan, [3]National Institute of Earth Physics, Magurele, Romania, [4]Computational Geodynamics Laboratory, Centro de Geociencias, Universidad Nacional Autónoma de México, Querétaro, Mexico, [5]National Research Institute for Earth Science and Disaster Prevention, Tsukuba, Japan

Abstract Although the thermal regime of the interface between two overlapping subducting plates, such as those beneath Kanto, Japan, is thought to play an important role in affecting the distribution of interplate and intraslab earthquakes, the estimation of the thermal regime remains challenging to date. We constructed a three-dimensional (3-D) thermal convection model to simulate the subduction of the Pacific plate along the Japan Trench and Izu-Bonin Trench, including the subduction of the Philippine Sea beneath Kanto and investigated the slab thermal regime and slab water contents in this complex tectonic setting. Based on the subduction parameters tested in generic models with two flat oceanic plates, a faster or thicker plate subducting in a more trench-normal direction produces a colder slab thermal regime. The interplate temperature of the cold anomaly beneath offshore Kanto was approximately 300°C colder than that beneath offshore Tohoku at a same depth of 40 km and approximately 600°C colder at a depth of 70 km. The convergence between the two subducting plates produces an asymmetric thermal structure in the slab contact zone beneath Kanto, which is characterized by clustered seismicity in the colder southwestern half. The thermo-dehydration state of the mid-ocean ridge basalt near the upper surface of the subducted Pacific plate controls the interplate seismicity beneath the Kanto-Tohoku region according to the spatial concurrence of the thermo-dehydration and seismicity along the megathrust fault zone of the subducted Pacific plate.

1. Introduction

Numerical simulation of the geodynamic process in subduction zones has been effectively applied in various geodynamic, tectonic, and geochemical studies over the last four decades [*Jacoby*, 1976; *Jacoby and Schmeling*, 1982; *OzBench et al.*, 2008; *van Keken et al.*, 2008; *Gerya*, 2011]. In general, there are currently two approaches to modeling a subducting plate [*Honda and Yoshida*, 2005; *Honda*, 2008; *Morishige et al.*, 2010]. One involves kinematic models, in which the geometry and movement of the subducting plate are imposed [*McKenzie*, 1967, 1968; *Hasebe et al.*, 1970; *Buttles and Olson*, 1998; *Kneller and van Keken*, 2007, 2008], and the other involves more dynamic models, in which the parameters are self-consistently determined [*Sleep and Toksöv*, 1971; *Kincaid and Olson*, 1987; *Gurnis and Hager*, 1988; *Funiciello et al.*, 2003; *Schellart et al.*, 2007; *Morra et al.*, 2006, 2009; *Duarte et al.*, 2013]. Provided that the domain of the oceanic slab has no significant motion (trench retreat, advance, or trench-parallel motion) or deformation during the process of subduction, a kinematic model can be an efficient tool for investigating the plate thermal regime using three-dimensional (3-D) simulations [e.g., *Morishige et al.*, 2010].

Models can also be classified in terms of dimensions, namely, two-dimensional (2-D) versus 3-D models. Previously, 2-D models have been used to study the dynamics in continental subduction channels and the interior of continental collision zones [e.g., *Enns et al.*, 2005; *Schmeling et al.*, 2008; *Ribe*, 2010], as well as to study the subduction-induced mantle flow near slab edges and curved slab surfaces [e.g., *Li et al.*, 2013; *Schellart and Moresi*, 2013]. Additionally, 2-D models have also been used to simulate the slab thermal structure to investigate dehydration reactions [*Peacock and Wang*, 1999; *van Keken*, 2003; *Manea et al.*, 2004, 2005], slab deformation under stress [*Wang et al.*, 2004], *P-T* paths and slab dehydration types [*Hacker et al.*, 2003a; *Peacock et al.*, 2005; *van Keken et al.*, 2011], heat flow effects [*Wada et al.*, 2008; *Wada and King*, 2015], and

seismic coupling [*Abers et al*., 2013]. In these models, temperature, pressure, metamorphism, and slab dehydration play important roles in generating intermediate-depth earthquakes. Among these parameters, the temperature is considered a critical factor because most of the dehydration processes are temperature- and pressure-dependent [e.g., *Omori et al*., 2009]. *Schellart and Moresi* [2013] ran both 2-D and 3-D subduction models and found that 2-D models can be used as an approximation of 3-D models for wide subduction zones. Some studies have attempted to estimate the thermal structure in specific convergent zones, such as Kanto, northeast Japan, southwest Japan, Kyushu, and Cascadia [e.g., *Hacker et al*., 2003b; *Yamasaki and Seno*, 2003; *Yoshioka et al*., 2008, 2013, 2015; *Wada and Wang*, 2009].

A number of 3-D analogue and numerical models have been developed in recent years to study a single isolated plate subducted into a vertically confined mantle [*Tackley*, 1998; *Funiciello et al*., 2003; *Lassak et al*., 2006; *Stegman et al*., 2006, 2010a, 2010b; *Schellart et al*., 2007; *Goes et al*., 2008; *Capitanio and Morra*, 2012; *Li and Ribe*, 2012; *Manea et al*., 2012]. Some subduction modeling studies are strictly limited to the upper mantle [*Funiciello et al*., 2008; *Schellart*, 2004; *Duarte et al*., 2013; *Chen et al*., 2016]. In some studies, 3-D time-evolving models were employed to investigate the finite strain fields associated with specific morphologies [e.g., *Kneller and van Keken*, 2007, 2008; *Jadamec and Billen*, 2010], seismic anisotropy and evolving crystallographic preferred orientation [e.g., *Russo and Silver*, 1994; *Faccenda and Capitanio*, 2012, 2013], and the poloidal and toroidal mantle flow patterns around the slab leading edge and lateral boundaries during trench retreat and advance [e.g., *Smith et al*., 2001; *Christensen et al*., 2003; *Strak and Schellart*, 2014, 2016]. *Zhu et al*. [2010] and *Yoshida et al*. [2012] investigated trench motion by imposing a trench retreat velocity and moving slab boundaries through their 3-D time-evolving thermal models. *Wada et al*. [2015] assumed a slab-mantle decoupling depth in their thermal model and explored the mantle wedge flow pattern and thermal structure in Hokkaido and northeast Japan around the hinge of the subducted Pacific plate.

For the subduction tectonic setting examined in this study, *Mishin et al*. [2008] performed 2-D numerical experiments by using a coupled petrological-thermomechanical approach based on a finite difference method. *Yoshioka et al*. [2015] constructed a 2-D thermal convection model to investigate the subduction of two oceanic plates and the resulting low heat flow in Kanto, central Japan, and found that the thermally estimated seismogenic zone corresponded well to the fault planes of historical megathrust earthquakes.

However, the 3-D kinematic simulation of complex subduction systems, such as that in Kanto in central Japan, has not been thoroughly studied in terms of the interplate thermal regime. Thus, the goal of this study is to better understand the thermal regime in a rather complex tectonic setting. Therefore, we developed a 3-D thermal convection model based on Stag3D [*Tackley and Xie*, 2003] and investigated the effects of different subduction parameters, such as the convergence rate, subduction history, and subduction obliquity.

The interplate coupling between the Pacific (PAC) and Philippine Sea (PHS) plates beneath Kanto may generate ongoing deformation in the slab contact zone [*Uchida et al*., 2010]. The down-dip limit of the strongly coupled interplate zone as inferred from thrust-type earthquakes on the PAC plate beneath Kanto is 30 km deeper than that beneath Tohoku. This difference is probably caused by a lower temperature environment resulting from the overlapping of the two plates and the consequent thermal shielding of the PAC plate from the hot mantle wedge [*Nakajima et al*., 2009a]. Many studies on laboratory experiments [e.g., *Segall et al*., 2010; *Ikari et al*., 2013], dynamic numerical modeling [e.g., *Abers et al*., 2013], seismic tomography [e.g., *Zhao*, 2012], and slow earthquakes [e.g., *Obara and Kato*, 2016] have shown that the presence of high pore pressure fluids can induce aseismic slip and/or tectonic tremors. Some studies have further suggested that slow-slip events can potentially trigger large earthquakes in northeastern Japan [*Kato et al*., 2012; *Uchida et al*., 2016]. To further investigate the subduction process in this complex subduction setting, we prescribed an appropriate dip angle, a convergence rate, and the boundary conditions in the generic models (hereafter referred to as the models with two flat oceanic plates), as illustrated in Figure 1. We also constructed a realistic model of the Philippine Sea-Pacific subduction setting (model 12), taking into account the plate geometries, slab thicknesses, subduction histories, and subduction velocities of the PAC and PHS plates, to estimate the thermal regime.

2. Methods and Models

Assuming an inelastic liquid approximation, the governing equations for calculating temperature, flow velocity, and pressure are the equations describing the conservations of mass, momentum, and energy [e.g., *Yoshioka and Murakami*, 2007; *Ji et al*., 2016]

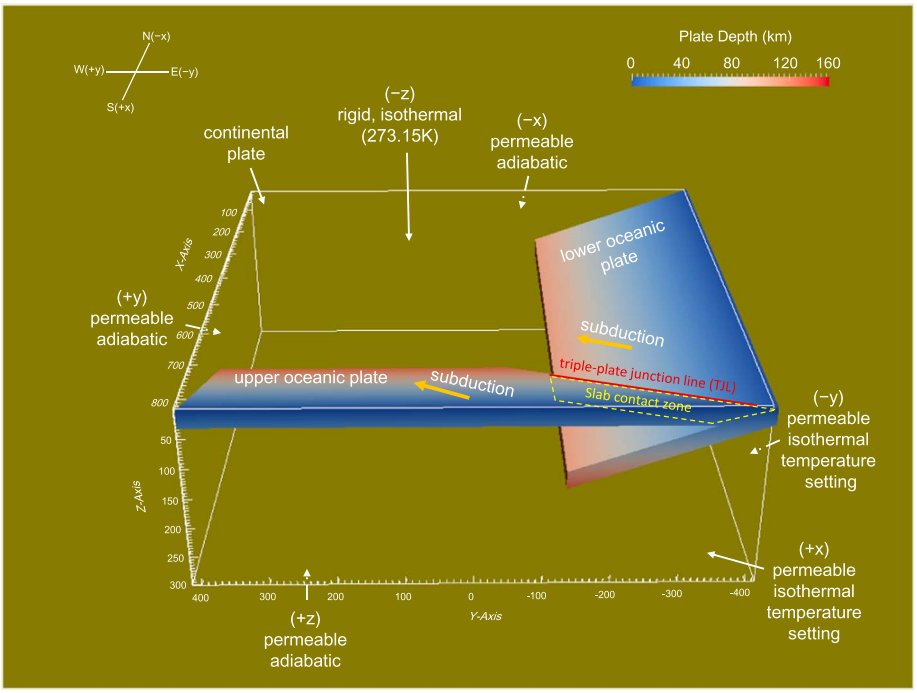

Figure 1. Boundary conditions for a 3-D numerical model of the subduction of two oceanic plates (generic models). The left, northward dipping oceanic plate is the overriding oceanic plate, and the right, westward dipping oceanic plate is the lower plate. The color of the oceanic plates indicates depth, and the orange arrows indicate example plate convergent velocities. The thin red line indicates the triple-plate junction line (TJL). The slab contact zone between the two oceanic plates is also marked (the area surrounded by yellow dashed lines).

$$\nabla \cdot \{\rho_s(z, T_s)\mathrm{v}\} = 0, \tag{1}$$

$$-\frac{\partial P}{\partial x_i} + \frac{\partial \tau_{ij}}{\partial x_j} - \delta_{i3}\rho_s g a_0 (T - T_s) = 0, \tag{2}$$

$$\rho C_{p0}\left(\frac{\partial T}{\partial t} + \mathrm{v}\ \nabla T\right) = k\nabla^2 T + \tau_{ij}\dot{\varepsilon}_{ij} + \rho g a_0 T v_3 + \rho H_r, \tag{3}$$

where the 3-D Cartesian coordinates consist of (x_1, x_2, x_3). $\rho_s(z, T_s)$ is the density at depth z and temperature T_s, v is the flow velocity vector, P is the pressure deviation from hydrostatic pressure, τ_{ij} ($i,j = 1, 2, 3$) is the stress tensor, δ_{ij} is the Kronecker delta, a_0 is the reference thermal expansivity, ρ is the density; g is the gravitational acceleration, C_{p0} is the specific heat at constant pressure, T is the in situ temperature, v_i is the ith component of the flow velocity vector v, k is the thermal conductivity, $\dot{\varepsilon}_{ij}$ is the strain rate tensor, and H_r is the internal radioactive heating per unit mass. Equation (3) comprises an advection term $\rho C_{p0}\mathrm{v}\ \nabla T$, a thermal diffusion term $k\nabla^2 T$, a viscous dissipation term $\tau_{ij}\dot{\varepsilon}_{ij}$, and a radioactive heating term ρH_r. The model parameters followed the 3-D thermal model [*Ji et al.*, 2016]. T_s can be expressed as follows:

$$\frac{dT}{dx_3} = \frac{g a_0}{C_{P0}} T_s. \tag{4}$$

The density ρ depends on temperature:

$$\rho = \rho_s(z, T_s)[1 - a_0(T - T_s)]. \tag{5}$$

We incorporated the subduction of a second oceanic plate into the model with a defined subduction velocity. We assumed a subduction velocity of 2.5–7.5 cm/yr in the generic models (Models 1 to 11; see Table 1). The velocity components in a Cartesian coordinate system were given according to the subduction velocity and

Table 1. Model Parameters for the 11 Generic Models Related to Subduction of the Underlying Oceanic Plate

Model Number	Subduction Direction of the Underlying Oceanic Plate	Subduction Velocity of the Underlying Oceanic Plate (cm/yr)	Thickness of the Underlying Oceanic Plate (km)	Figure Numbers	Curve Number in Figure 5
1	N45°W	5.0	30	2c	1
2	N55°W[a]	5.0	30	2a, 2b	2
3	N35°W	5.0	30	2d	3
4	N45°W	2.5	30	2e	4
5	N45°W	7.5	30	2f	5
6	N45°W	5.0	15		6
7	N45°W	5.0	45	2g	7
8	N105°W	5.0	30		8
9	N90°W	5.0	30	2h	9
10	N75°W	5.0	30		10
11	N60°W	5.0	30		11

[a]Underlining indicates specific model parameter in each model.

the subduction direction on the upper surface of the oceanic plates, hypothesizing that the slab geometry is fixed:

$$v_x(x,y,z) = \frac{-2a(x,y)b(x,y)v_y + \sqrt{\{2a(x,y)b(x,y)v_y\}^2 - 4\left\{a(x,y)^2+1\right\}\left[\left\{a(x,y)^2+1\right\}v_y{}^2 - v^2\right]}}{2\left\{a(x,y)^2+1\right\}}, \quad (6)$$

$$v_y(x,y,z) = v_y, \quad (7)$$

$$v_z(x,y,z) = a(x,y)v_x + b(x,y)v_y, \quad (8)$$

with

$$a(x,y) = \frac{1}{2}\{Z(x+\Delta x,y) - Z(x-\Delta x,y)\}\frac{z_{\max}}{x_{\max}}, \quad (9)$$

$$b(x,y) = \frac{1}{2}\{Z(x+\Delta x,y+\Delta y) - Z(x+\Delta x,y) + Z(x-\Delta x,y) - Z(x-\Delta x,y-\Delta y)\}\ \frac{z_{\max}}{y_{\max}}, \quad (10)$$

where v is the total subduction velocity and $v_x(x,y,z)$, $v_y(x,y,z)$, and $v_z(x,y,z)$ are velocity components associated with subduction of the oceanic plate in the x, y, and z directions, respectively. Δ_x and Δ_y are the intervals of two neighboring nodes along the x and y axes, respectively. $x_{\max}$, $y_{\max}$, and $z_{\max}$ are the lengths of the model box along the x, y, and z axes, respectively (Figure 1). We imposed the subduction velocity on all nodes belonging to the subducting PAC and PHS plates. The frictional heating of the slab contact zone was not included in this study because the observed surface heat flow is abnormally low in Kanto [*Yoshioka et al.*, 2015] and because smooth megathrusts that produce great earthquakes, such as the Tohoku-oki event, tend to be weaker and therefore dissipate less frictional heat to the surface [*Gao and Wang*, 2014].

Viscosity η was defined by the viscous flow law for wet olivine [*Hirth and Kohlstedt*, 2003; *Burkett and Billen*, 2010]. The composite upper mantle viscosity for deformation at constant stress is

$$\eta_{\text{comp}} = \frac{\eta_{df}\eta_{ds}}{\eta_{df}+\eta_{ds}}, \quad (11)$$

where η_{df} and η_{ds} are the diffusion creep and dislocation creep viscosities for olivine, respectively. The general form of the viscosity law is given by

$$\eta_{df,ds} = \left(\frac{d^p}{A_0 C^r{}_{OH}}\right)^{\frac{1}{n}} \dot{\varepsilon}_E^{\frac{1-n}{n}} \exp\left(\frac{E_0 + P_l V_0}{n_0 R T_a}\right), \quad (12)$$

where $\dot{\varepsilon}_E = \left(\frac{1}{2}\dot{\varepsilon}_{ij}\dot{\varepsilon}_{ij}\right)^{\frac{1}{2}}$ is the square root of the second invariant of the strain rate tensor [*Ranalli*, 1995], T_a is the temperature including the adiabatic temperature gradient (3×10^{-4} K/m), R is the gas constant, and P_l is the lithostatic pressure defined by the adiabatic compressibility in the mantle:

Table 2. Model Parameters for Wet Olivine at Constant Water Content [*Hirth and Kohlstedt*, 2003; *Burkett and Billen*, 2010]

		Flow Law Parameters	
	Parameter	Diffusion Creep	Dislocation Creep
n_0	Stress exponent	1.0	3.5
A_0	Preexponential factor ($s^{-n}Pa^{-n}\mu m^{p}C_{OH}^{-r}$)	1.0	9.0×10^{-20}
E_0	Activiation energy (kJ/mol)	335	480
V_0	Activiation volume (m^3/mol)		
	Upper mantle	4.0×10^{-6}	11.0×10^{-6}
	Lower mantle	1.5×10^{-6}	-
d	Grain size(μm)		
	Upper mantle	10,000	-
	Lower mantle	40,000	-
p	Grain size exponent	3.0	-
C_{OH}	OH concertration ppm H/Si	1000	1000
r	C_{OH} exponent	1.0	1.2

$$P_l = -\frac{1}{\beta_a}\ln(1-\rho_s g\beta_a z), \tag{13}$$

where z is depth, ρ_s is the density, and the adiabatic compressibility $\beta_a = 4.3\times10^{-12}\cdot Pa^{-1}$ [*Turcotte and Schubert*, 2002]. The values of the model parameters for the diffusion and dislocation creep of olivine in equation (12) are tabulated in Table 2.

The size of the modeled region is $840\times840\times300$ km. The grid number is $96\times96\times96$, and the grid interval is 8.75 km horizontally and 3.13 km vertically. We tested the resolution and found that the calculated result for the thermal regime along the whole studied interface became comparatively stable when the mesh exceeded $72\times72\times72$. The average temperature variance of the entire model was $<5\%$ between meshes of $72\times72\times72$ and $84\times84\times84$, and $<1\%$ between meshes of $84\times84\times84$ and $96\times96\times96$. Hence, the mesh used in this study was considered sufficient for accurate interplate thermal estimation. In the generic models, the subducting PAC slab was assumed to dip to the west ($+y$), and the subducting PHS slab was assumed to dip to the north ($-x$), both with dip angles of nearly 20°. The boundary conditions in the 3-D model included a rigid and isothermal upper surface ($-z$), a permeable and adiabatic bottom ($+z$) and sidewalls ($-x$ and $+y$), and permeable and fixed-temperature trenchward sides ($+x$ and $-y$). The trenchward thermal structure followed the model GDH1 [*Stein and Stein*, 1992; *McKenzie*, 1967; *Grose and Afonso*, 2013]:

$$T(z,t_{oc}) = T_m\left[\frac{z}{d_0}+\frac{2}{\pi}\sum_{n-1}^{\infty}\frac{1}{n}\sin\left(\frac{n\pi z}{d_0}\right)\exp\left(\frac{-n^2\pi^2\kappa t_{oc}}{{d_0}^2}\right)\right], \tag{14}$$

where $T(z, t_{oc})$ is the temperature at depth z and age t_{oc} of the oceanic plate along the Nankai Trough, T_m is a lithospheric basal temperature, d_0 is the depth below which adiabatic heating is applied, and K is the thermal diffusivity. The initialization time was included, and a time-dependent thermal boundary condition was adopted for the model. Specific interplate decoupling depths were not incorporated into the model. The two oceanic slabs were immediately in contact with each other with no gaps in the slab contact zone. For generic Models 1 to 11 with flat slabs, the overriding oceanic plate had a subduction velocity of 5 cm/yr, a subduction direction of N45°W, and a slab thickness of 30 km. In contrast, the values of some parameters of the underlying oceanic plate were varied among the 11 models, as described in Table 1. In particular, the underlying oceanic plate was assigned seven subduction directions from N35°W (Model 3) to N105°W (Model 8) with an increments of ≤15° in Models 1–3 and 8–11 to identify the effects of subduction direction on the slab thermal regime. The thermal parameters reported by *Mishin et al.* [2008], including the subduction velocity and slab thickness, were also examined in Models 4–7. The results of the generic models are described in section 3 and shown in Figures 2–4, and the parameters are listed in Tables 2 and 3.

Furthermore, we applied the thermal model to the Philippine Sea-Pacific subduction setting from Kanto to Tohoku and obtained the results described in section 4. The young PHS plate is subducting northwestward

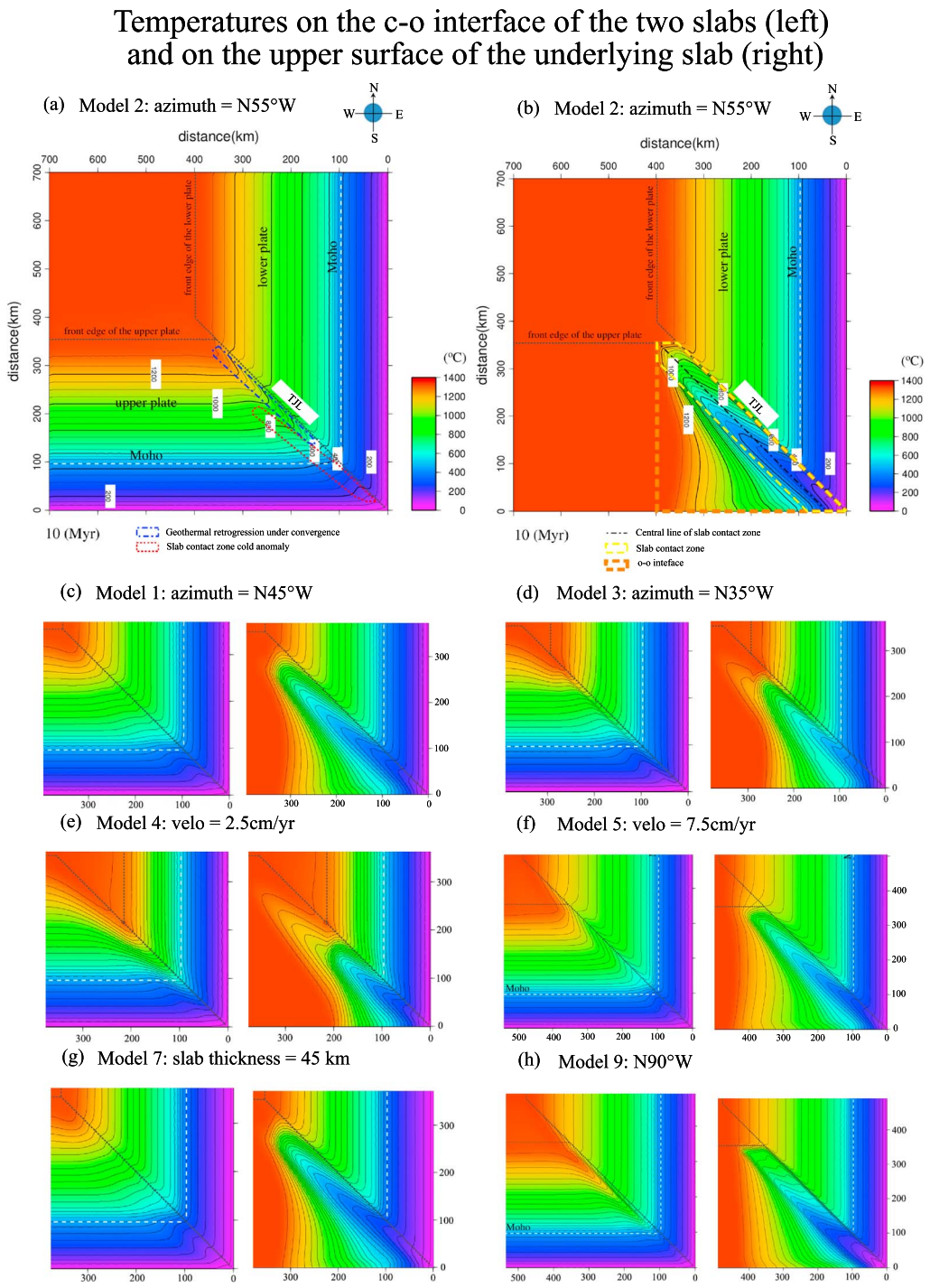

Figure 2. (a) Oceanic-continental interplate thermal regime for Model 2 after 10 Myr. For the two oceanic plates, the subduction velocities are 5 cm/yr, the dip angles are 20°, and the slab thicknesses are 30 km. The subduction directions are N45°W for the overriding oceanic plate and N55°W for the underlying oceanic plate (Nn°W denotes n° counterclockwise from north). The white dotted lines indicate the depth of the continental Moho. The zone circled with the red dotted line represents the slab contact zone cold anomaly (SCA). The zone circled with the blue dash-dotted line represents the geothermal retrogression. (b) Interplate thermal regime of the upper surface of the underlying oceanic plate in Model 2 after 10 Myr. The zone circled with the orange dashed line indicates the oceanic-oceanic plate interface (o-o interface) between the lower boundary of the overriding oceanic plate or mantle and the upper surface of the underlying oceanic plate. The zone circled with the yellow dashed line represents the slab contact zone. The o-o interface includes the upper mantle in addition to the crust of the oceanic plate; therefore, the o-o interface is larger than the slab contact zone. The blue dash-dotted line indicates the central axis of the slab contact zone. (c) Left, the oceanic-continental interplate thermal regime after 10 Myr; right, the interplate thermal regime of the upper surface of the underlying oceanic plate after 10 Myr for Model 1. The values of the model parameters are shown in Table 1. (d) The same as Figure 2c except for Model 3. (e) The same as Figure 2c except for Model 4. (f) The same as Figure 2c except for Model 5. (g) The same as Figure 2c except for Model 7. (h) The same as Figure 2c except for Model 9.

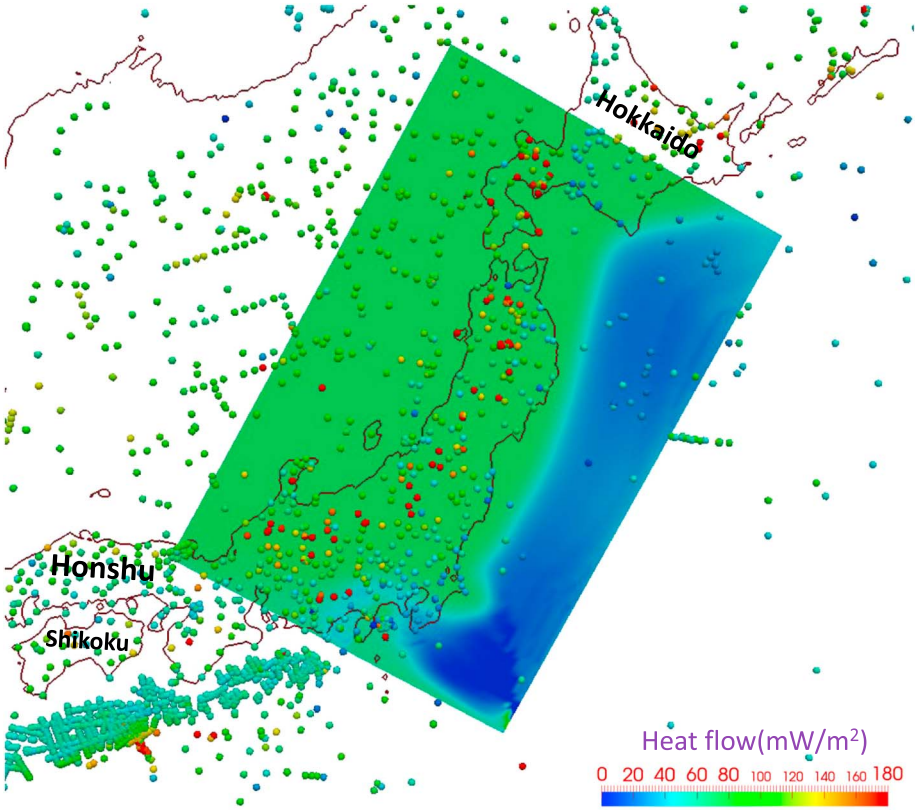

Figure 3. Spatial distributions of observed (colored circles) and calculated (colored boxes) surface heat flow from Kanto to Tohoku. The observation of surface heat flow includes the Global Heat Flow Database [*Pollack et al.*, 1993], bottom-simulating reflectors [*Ashi et al.*, 1999, 2002], terrestrial boreholes and marine heat probes [*Tanaka et al.*, 2004; *Yamano*, 2004], and Hi-net boreholes [*Matsumoto*, 2007].

beneath the Okhotsk (North American) plate along the Sagami Trough, and the old PAC plate is subducting westward beneath both the PHS and Okhotsk (North American) plates along the Japan Trench. The PHS and the PAC plates overlap beneath Kanto. Unlike the situation in the generic models, we considered the actual geometries of the two oceanic plates based on seismic tomography of the PAC plate [*Nakajima et al.*, 2009b] and the PHS plate [*Nakajima and Hasegawa*, 2007]. In the model of the Philippine Sea-Pacific subduction setting (Model 12), the subduction velocity of the PAC plate was approximated to be 8–10 cm/yr (Table 4), and the subduction direction with respect to the Okhotsk (North American) plate was estimated to be N70°W, according to Mid-Ocean Ridge Velocity (MORVEL) [*DeMets et al.*, 2010] and NNR-MORVEL56 [*Argus et al.*, 2011]. The PHS plate is subducting at approximately 3–4 cm/yr in the direction of approximately N50°W along the Sagami Trough. In the late Pliocene-Holocene volcanic arc stage, accelerated subduction of the PHS plate began at approximately 4 Ma [*Kimura et al.*, 2005]. *Takahashi* [2006] proposed that the location of the Euler pole of the PHS plate shifted at 3 Ma from east of the triple junction to the northeast of Hokkaido, Japan. Hence, we hypothesize that the PHS plate subducted with respect to the Eurasian plate before 3 Ma and with respect to the Okhotsk (North American) plate after 3 Ma. The age of the PAC plate is considered to be approximately 130 Myr [*Sdrolias and Muller*, 2006], and its thickness is nearly 85 km. The age of the PHS plate beneath Kanto is considered to be ~40 Myr [*Nakajima and Hasegawa*, 2007]. In this study, we assumed that the PHS plate was 40 Myr old and had a slab thickness of nearly 30 km. The subduction history of the PAC plate was considered to be at least 20 Myr, which is long enough to reach a mature stage that approximates a steady state, whereas the subduction history of the PHS plate was considered to be 9 Myr, which is the time required for the leading edge to reach its current location after experiencing rotation and oblique subduction. The Okhotsk (North American) plate was considered to be fixed with respect to the Amurian plate. The adopted subduction histories for the two plates ensured that the calculated plate geometry at 0 Ma matched the current plate geometry based on seismic tomography. The values of the model parameters are listed in Table 4.

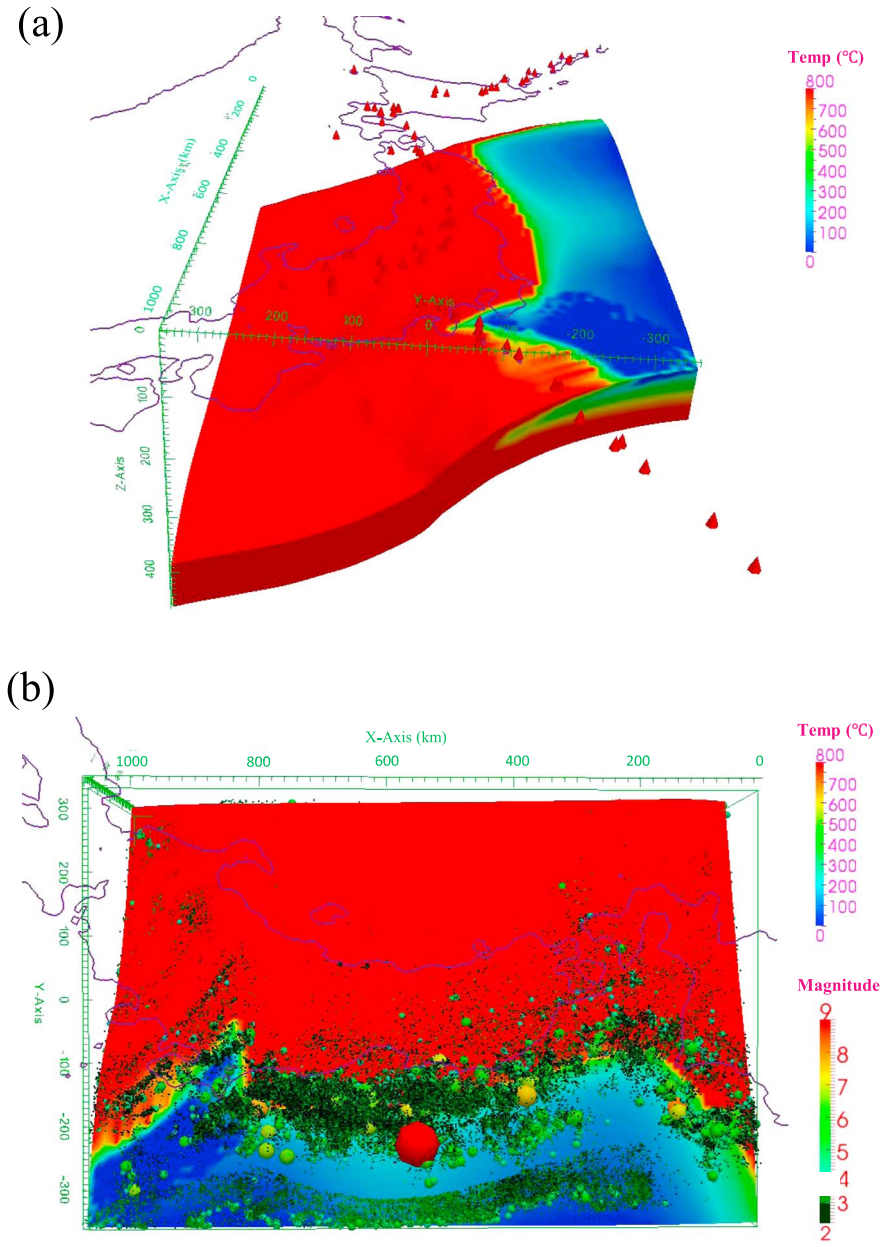

Figure 4. (a) Map view perspective of the 3-D temperature distribution of the subducted PAC and the PHS plates beneath northeastern Japan. The portion with a temperature over 800°C was saturated in red. The red cones indicate active volcanoes. (b) Map view perspective of the 3-D temperature distribution on the upper surface of the Pacific plate with a hypocenter distribution of earthquakes with magnitudes greater than 4.0 (small spheres) and from 2.0 to 4.0 (small dots). The hypocenters were taken from the JMA unified hypocenter data catalog (1 October 1997 to 28 February 2015). The largest red sphere indicates the 2011 Tohoku-oki earthquake (*M*9.0).

The obtained slab temperature and depth-dependent pressure were subsequently applied to calculate the water content inside the subducting oceanic plate via the phase diagrams of mid-ocean ridge basalt (MORB) [*Omori et al*., 2009] and ultramafic minerals [*Hacker et al*., 2003a]. Compared with the previous studies, which have mostly focused on a vertical 2-D water content distribution, this study provides a 3-D perspective of the slab dehydration regime, resulting in an approximate interplate water content map beneath Kanto and Tohoku. Finally, the loci of earthquake hypocenters from the Japan Meteorological Agency (JMA) during the period from 1 October 1997 to 28 February 2015 were compared with the obtained simulation results.

Table 3. Values of Model Parameters for 3-D Numerical Simulation of Subduction of Two Oceanic Plates

Symbol	Parameters	Value	Units
ρ_0	Standard density	3.3×10^{3}[a]	kg/m^3
T_0	Temperature difference between top and bottom of the model	1.6×10^{3}	K
k_0	Standard thermal conductivity	2.9[b]	W/(m▪K)
Hr	Radioactive heat generation rate in the mantle	2.245×10^{-13}[a]	W/m^3
C_{p0}	Standard specific heat at constant pressure	1.2×10^{3}[a]	J/(kg▪K)
κ_0	Standard thermal diffusivity	7.6×10^{-7}[c]	m^2/s
η_0	Standard viscosity	1.0×10^{20}[b]	Pa▪s
α_0	Standard thermal expansion	3.0×10^{-5}[d]	/K
v_0	Subduction velocity	2.5 ~ 7.5	cm/yr

[a] *Wang et al.* [1995].
[b] *Christensen* [1996].
[c] *Yoshioka and Murakami* [2007].
[d] *Iwamori* [1997].

3. Simulation Results for the Generic Thermal Models

In the generic models with two flat oceanic plates, the interface between the continental lithosphere and the oceanic plates is referred to as the c-o interface, and the interface between the two oceanic plates is referred to as the o-o interface. The contact zone between the two slabs appears in the uppermost portion of the o-o interface. The uppermost edge of the slab contact zone is referred to as the triple-plate junction line (TJL) (Figure 1).

Although the subduction direction of the underlying oceanic plate (N45°W) in Model 1 is parallel to that of the overriding oceanic plate, we selected Model 2 (N55°W) as the best representative to discuss due to its similarity to the real subduction azimuths in Kanto. Figures 2a and 2b show the temperature distributions on the c-o interface and the upper surface of the underlying oceanic plate, respectively. A cold zone with a width of approximately 50 km is present on the lower left side of the TJL in Figure 2a (the region circled with red dotted lines). A maximum temperature decrease of nearly 50°C compared to the rest of the c-o interface at the same depth is also observed and is hereafter referred to as the "slab contact zone cold anomaly" (SCA). We find that the SCA is attributable to the oblique cold anomaly in the slab contact zone, which is circled by yellow dashed lines in Figure 2b.

For comparison, the results of Models 1, 3, 4, 5, 7, and 9 (Figure 2) are also shown. When the subduction direction of the underlying oceanic plate was changed from N45°W (Figure 2c) to other directions, the peak temperature drop of the SCA remained at nearly 50°C, but its coldest location on the c-o interface (peak) moved closer to or farther from the TJL (Figure 2). When the underlying oceanic plate had a subduction direction of N90°W (Figure 2h), the coldest temperature was farthest away from the TJL, and the peak temperature drop diminished to a level that is hard to identify. Therefore, the peak temperature drop reached a maximum in a direction of approximately N45°W–N55°W (Figures 2a and 2c), and the coldest nucleus appeared in the slab contact zone (Figures 2b and 2c, right). Accordingly, the changes in the subduction direction of the underlying oceanic plate altered the location and amplitude of the peak cold zone of the SCA, as can be observed in the right panels of Figures 2d–2h.

Table 4. Parameters for the Realistic Model (Model 12) in Kanto and Tohoku, Japan

Plate	Current Age (Myr)	Slab Thickness (km)	Subduction Direction	Subduction Velocity (cm/yr)	Subduction History
PAC	132 Myr[a]	85[a,b]	N71.6°W[c]	9.7[c]	20 Ma ~ 0 Ma
PHS (9 Ma–3 Ma)	40 Myr[a]	30[a,b]	N26.5°W[c]	5.4[c]	9 Ma ~ 3 Ma
PHS (3 Ma–0 Ma)			N59.8°W[c]	5.4[c]	3 Ma ~ 0 Ma

[a] *Muller et al.* [2008].
[b] *Yoshii* [1975].
[c] *DeMets et al.* [2010].

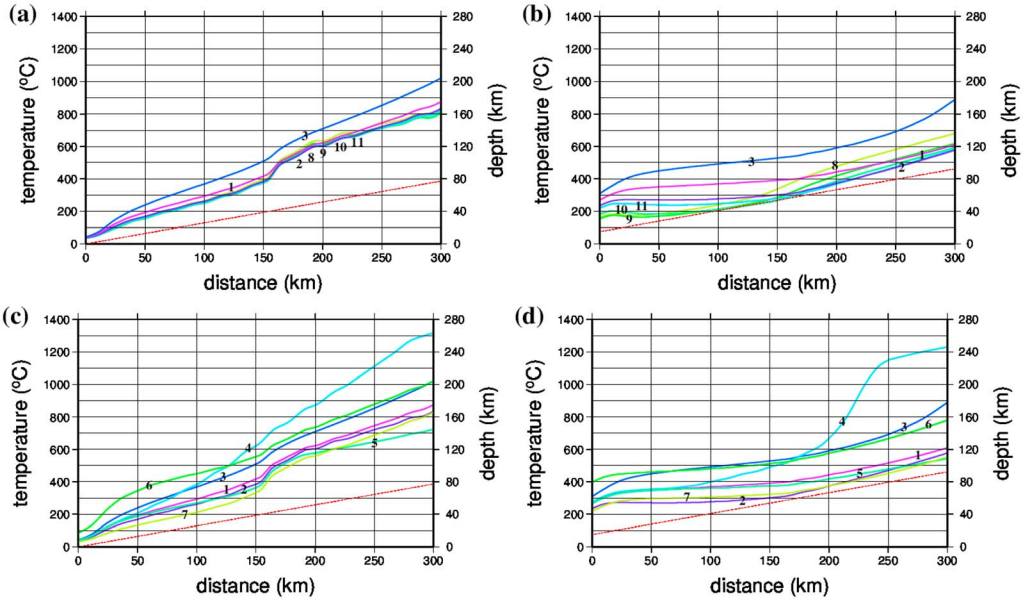

Figure 5. (a) Temperature profiles along the TJL line for Models 1–3 and 8–11. The curve number represents the number of the model (see Table 1). These models have the same subduction velocities and slab thicknesses but different subduction directions: N45°W, N55°W, N35°W, N105°W, N90°W, N75°W, and N60°W, respectively. The red dotted line represents depths along the profiles. (b) Temperature profiles along the central line of the slab contact zone (Figure 2b) for Models 1–3 and 8–11. (c) Temperature profiles along the TJL line for Models 1–7 (otherwise the same as Figure 5a). Curves 1–7 represent subduction directions of N45°W, N55°W, and N35°W; subduction velocities of 2.5 cm/yr and 7.5 cm/yr; and slab thicknesses of 15 km and 45 km, respectively. (d) The temperature profiles along the central line of the slab contact zone for Models 1–7 (otherwise the same as Figure 5b).

When we reduced the subduction velocity of the underlying oceanic plate from 5 cm/yr (Figure 2c) to 2.5 cm/yr (Figure 2e), the SCA weakened and seemed to disappear at depths greater than the continental Moho. Thus, halving the subduction velocity of the underlying oceanic plate resulted in a nearly halved cold effect; in other words, the temperature perturbation in this model was half that of the reference model. When the thickness of the underlying oceanic plate was assumed to be 15 km instead of 30 km, the SCA disappeared. For a slab thickness of 45 km, the peak temperature drop was elevated to nearly 100°C (lower right region near TJL in Figure 2g, left), suggesting that a thicker subducting plate produces a colder SCA (Figure 2g, right).

Consequently, faster and more trench-normal subduction of a thicker lower oceanic plate contributes to a colder slab contact zone if the area of the slab contact zone is fixed. Further quantitative analyses of the detailed parameter-related thermal regime are presented in section 5.1 (Figure 5).

4. Simulation Results for the Kanto-Tohoku Thermal Model

4.1. Calculated Surface Heat Flow and Observations

The anomalously low fore-arc surface heat flow is greatly affected by the oceanic plate subducting beneath the fore-arc zone, especially at depths shallower than 50 km. In the case of the two overlapping slabs beneath Kanto, low heat flow in the fore-arc was also observed [*Yoshioka et al*., 2015]. We used the least variance method to compare the calculated results with observations from the Global Heat Flow Database [*Pollack et al*., 1993], terrestrial boreholes and marine heat probes [*Tanaka et al*., 2004; *Yamano*, 2004], and Hi-net boreholes [*Matsumoto*, 2007]. Although the effects of regional crustal radioactive heating on heat flow values remain unclear at present, a relatively satisfying solution (colored box) fitting the observations (colored spheres) in the Kanto-Tohoku region was calculated (Figure 3). The observations and calculated results were generally consistent with each other, except in some volcanic arcs, coastal regions, and inland Hokkaido. However, if we consider the regional tectonic settings affecting the surface heat flow and the fact that the horizontal spatial resolution is 15 km, the calculated results basically meet the requirements for evaluating the interplate thermal regime in these regions.

4.2. Thermal Regime and Dehydration Near the Upper Surface of the PAC Plate

Based on the calculated thermal regimes depicted in Figures 4a and 4b, we identified a remarkable shallow cold interplate zone on the upper surface of the PAC plate (Figure 4a). The 2011 Tohoku-oki earthquake (*M*9.0) and a large number of M4-class earthquakes are distributed along the western edge of the cold belt, which represents a transition zone spanning temperatures from nearly 300°C to 600°C. This temperature window corresponds to the MORB phase transition from blue/greenschist to amphibolite or from lawsonite amphibole eclogite to amphibole eclogite [*Hacker et al*., 2003a; *Omori et al*., 2009]. Therefore, the temperature of the colder region inside the slab contact zone offshore Kanto was nearly ~300°C lower than the temperature offshore Tohoku at the same depth of 40 km and approximately ~600°C colder than that beneath Tohoku at a depth of 70 km (Figure 4b).

5. Discussion

5.1. Effects of Subduction Parameters on the Thermal Regime of the Slab Contact Zone

The subduction thermal parameters in the slab contact zone were investigated in detail in the generic models. For example, when the subduction direction of the underlying oceanic plate was shifted to N90°W from N45°W, the temperature distribution of the slab contact zone changed so that the coldest axis of the slab contact zone was aligned with the new subduction direction of the underlying oceanic plate, i.e., westward for the westward-dipping plate (Figure 2h, right). The temperature distribution in the slab contact zone becomes symmetrical when the two oceanic plates subduct in the same direction (N45°W) (Figure 2c, right). Therefore, the distribution of the coldest nucleus in the slab contact zone is consistent with the direction of subduction of the underlying oceanic plate.

When the subduction direction of the underlying oceanic plate was gradually shifted to the west or north of N45°W, the cold anomaly at the TJL gradually weakened and a hot anomaly to the west of the TJL appeared (hereafter referred to as "geothermal retrogression") when the subduction direction was N90°W (Figure 2h, left). When the subduction directions of the two slabs differed considerably (Figures 2a and 2h, left), a geothermal retrogression (the zone circled by the blue dash-dotted line in Figure 2a) developed on the c-o interface near the TJL. This geothermal retrogression is considered to be the result of the confined mantle wedge below the continental lithosphere. Subduction of a faster or thicker oceanic plate weakens the geothermal retrogression, whereas subduction of a slower or thinner oceanic plate results in the opposite effect (Figures 2f, left and 2g, left). Consequently, the geothermal retrogression is also affected by the subduction obliquity, subduction velocity, and thickness of the lower oceanic plate.

Furthermore, quantitative analysis of temperature profiles along the TJL and along the central lines of the slab contact zone was performed, as shown in Figure 5. Figures 5a and 5b show the relationships identified among subduction direction, the SCA, and slab-convergent geothermal retrogression. The seven curves indicate the temperature variation along the TJL (Figure 5a) and the central line of the slab contact zone (Figure 5b) for the models with underlying oceanic plate subduction directions ranging from N105°W to N35°W. In Figure 5a, six curves (Models 1, 2, and 8–11) are clustered and have differences within 100°C along the TJL. Their similarity indicates that the c-o interface temperature of the overriding oceanic plate was the same in these models. When the subduction direction was changed to N35°W from N45°W, the temperature along the TJL increased by 0–200°C and the cold anomaly along the TJL weakened markedly (Model 3) compared to the other models. Figure 5b shows the temperature profiles along the central line of the slab contact zone for various models. Based on the group of curves on the left side of the graph, the minimum temperatures correspond to the subduction direction of N90°W (Model 9) at a depth of $<$40 km (i.e., a horizontal distance of $<$100 km) and to the subduction direction of N55°W (Model 2) at a depth of $>$70 km. Curve 3, which differs from the other curves, represents the most oblique subduction among the seven models. The maximum temperature variation among the seven models along the central line of the slab contact zone, i.e., the difference between the coldest slab contact zone (Model 9, with nearly trench-normal subduction) and the hottest slab contact zone (Model 3, with the most oblique subduction), was approximately 300°C at depths of 30 to 100 km. In addition, the central line of the slab contact zone in the model with a subduction direction of N105°W (Model 8) was nearly 100°C hotter than that in the model with a subduction direction of N55°W (Model 2) (Figure 5b) at depths greater than 50 km, i.e., at a down-dip distance of $>$150 km.

Figures 5c and 5d show the calculated temperature distributions along the TJL and the central axis of the slab contact zone, respectively. The plots are similar to those in Figures 5a and 5b, but for a different combination of the models. Instead of Models 8–11, which are characterized by a westward subduction direction, Figures 5c and 5d show results for Models 4–7, which have different subduction velocities and different oceanic plate thicknesses. Greater obliquity is effectively equivalent to slower subduction (Model 4) or a thinner, younger underlying oceanic plate (Model 6). Curve 4 features the highest values and the steepest slope among the curves beyond a subduction distance of 150 km due to its halved subduction rate of 2.5 cm/yr (Table 1), leading to an insufficient subduction distance of less than 150 km in the down-dip direction. Although the temperatures along the TJL were sensitive to subduction velocity, subduction azimuth, and slab thickness, they were most sensitive to changes in the subduction velocity beneath the continental Moho. The curves of Models 6 and 7 in Figure 5d show that the temperature profiles along the central line of the slab contact zone were sensitive to slab thickness, and the temperature variation between these two curves along the central line of the slab contact zone was approximately 200°C. In addition, the high temperature of Model 4 relative to Model 5 at depths greater than 70 km was attributed to a lower subduction velocity.

The quantitative analyses supported the inference that subduction velocity, subduction obliquity, and slab thickness play key roles in influencing the thermal regime of the slab contact zone. The results agreed with the 2-D thermal modeling results of *Mishin et al*. [2008], who concluded that the parameters of the subduction zones depend on the relative plate motion velocities, slab ages, and length of the overriding oceanic plate. However, this study further demonstrated that subduction obliquity is also a key factor and that the overlying oceanic plate tends to control the thermal regime in complex subduction zones.

5.2. Relationships Among Thermal Regime, Seismic Velocity Structure, and Interplate Seismicity in the Slab Contact Zone

Nakajima and Hasegawa [2006], *Hasegawa et al*. [2007], and *Nakajima et al*. [2009a, 2009b] revealed a northwest-southeast (NW-SE) trending linear alignment of seismicity near the southwestern periphery of the slab contact zone at a depth range of 60–120 km near the upper surface of the subducted Pacific plate beneath Kanto. This seismicity correlates spatially with a narrow low-velocity zone imaged beneath Kanto within the subducted plate over a distance of ~150 km landward from the Sagami Trough (Figure 6 a) [*Nakajima et al*., 2009a, 2009b]. A belt-like low *S*-wave velocity zone at depths of 80–120 km extends in the NNW-SSE direction from the Sagami Trough at an initial orientation of N45°W, which then rotates gradually counterclockwise to N70°W north of Tokyo (the yellow area in Figure 6a shows the configuration of the slab contact zone). The clustered distribution of seismicity at depths of 60–120 km to the southwest of the slab contact zone (the zone circled with the solid red line in Figure 6a) also exhibits a similar change in orientation.

In contrast, less clustered seismicity is present along the northern edge of the slab contact zone (Figures 4b and 8a, which is also shown in *Nakajima et al*. [2009b]), even though the megathrust fault zone is acknowledged to be a thermally controlled active seismic zone at a depth of 80 km in Tohoku [*Kita et al*., 2006] (the zone circled with the dashed red line in Figure 6a). In the northern part of the slab contact zone, evidence for high seismic attenuation in the serpentinized subducting plate was found, likely due to ductile deformation (rather than brittle failure) facilitated by fluids supplied along the plate boundary [*Nakajima*, 2014]. This finding is consistent with the thermal asymmetry of the slab contact zone found in this study showing that the southwestern slab contact zone is colder than the northern counterpart (Figure 2). *Hasegawa et al*. [2007] found that the upper plane of the seismic belt beneath Kanto is nearly parallel to the down-dip edge of the slab contact zone.

We compared our results with the anomalous NW–SE-trending alignment of high seismicity that occurs near the southwestern periphery of the slab contact zone at depths of 60–120 km [*Nakajima et al*., 2009b]. In Kanto, the TJL lies along the northern edge of the slab contact zone near profile A-A′ in Figure 6a, and the hypocenters of earthquakes in this region are 40 km deeper than those beneath Tohoku (Figures 4b and 8a). The temperature difference of ~300°C associated with the cold slab contact zone likely accounts for the observed low surface heat flow of ~50 mW/m^2. This finding was also noted by *Yoshioka et al*. [2015], who investigated the thermal effects of the subduction of the PHS and PAC plates beneath Kanto. The difference in the subduction velocities between the two oceanic plates might result in the accumulation of strain in the slab contact zone. Creep behavior could also occur due to the

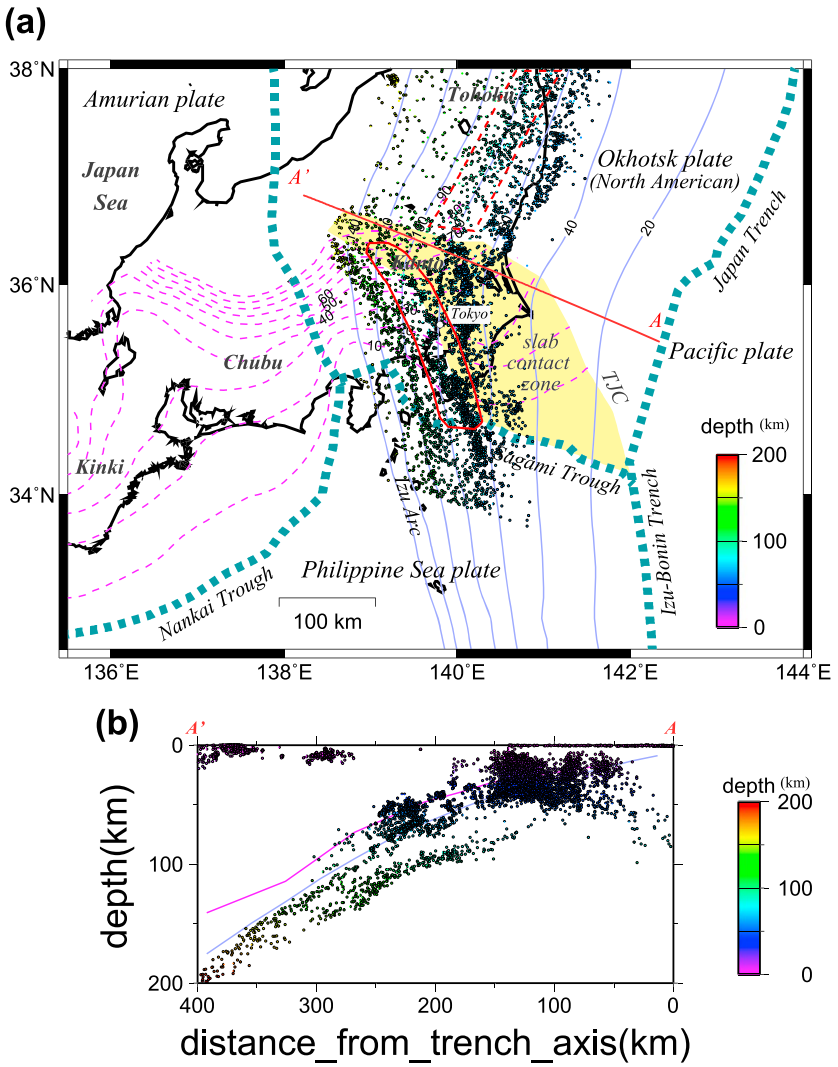

Figure 6. (a) Hypocenter distribution of earthquakes with magnitudes greater than 2.0 during the period of 1 October 1997 to 28 February 2015 (observed by the Japan Meteorological Agency (JMA)). Hypocenters within a vertical distance of 20 km below and 10 km above the upper surface of the PAC slab at depths of 60–160 km beneath the region of Kanto and southern Tohoku are plotted. The colors of the dots indicate the depth of the hypocenters. The thick blue dotted lines are the plate boundaries. Isodepth contours of the upper surfaces of the PAC and the PHS plates by *Nakajima et al.* [2009a, 2009b] are indicated with blue solid and pink dashed curves, respectively. The yellow strip indicates the area of the slab contact zone where the lower surface of the Philippine Sea slab comes into contact with the upper surface of the Pacific slab [*Nakajima et al.*, 2009b]. The zone circled with a red solid line along the southwestern edge of the slab contact zone has a more distinct seismicity cluster than the northern edge of the slab contact zone. The zone circled by the red dashed line along the isodepth contour of approximately 80 km beneath Tohoku represents the clustered seismic belt associated with the subduction of the PAC plate [*Nakajima et al.*, 2009b]. (b) Vertical cross section of the seismicity within a one-side width of 20 km along the profile A-A′ on the northern edge of the slab contact zone in Figure 6a. The earthquakes recorded during the same period as those in Figure 6a are plotted. The pink and blue lines indicate the upper surfaces of the PHS and the PAC plates, respectively.

structural complexity and could potentially alter the geometry of the oceanic plates or the relative plate motion between the two oceanic plates in this region. Based on the geometry of the two plates, the slab contact zone is currently understood to be the result of the geodynamic process of interplate coupling. According to MORVEL [*DeMets et al.*, 2010], the absolute value of the difference in subduction directions between the PAC and PHS plates with respect to the Okhotsk (North American) plate varies from ~10° to 20° at the slab contact zone beneath Kanto to a depth of 100 km. Possible processes for releasing the built-up stress include deformation, fracturing, and the breakdown of hydrous materials in a saturated

layer in one of the subducting plates. *Uchida et al*. [2010] supposed that certain features of the PHS plate, such as the relative flatness at its northeastern limit and the concave bend, are likely the effects of ongoing deformation related to the interaction with the underlying thick PAC plate. The geometry of the slab contact zone beneath Kanto (Figure 4a) is more curved than that in the generic models (Figure 2b).

Compared to the results of *Nakajima et al*. [2009a], the down-dip limit of the interplate thrust-type earthquakes on the Pacific plate beneath Kanto in this work was deeper by 30 km, presumably due to a local lower temperature environment. For the Pacific plate, with a subduction velocity of 8–10 cm/yr and a slab thickness of approximately 85 km, we estimated that the temperature of the plate interface adjacent to the slab contact zone is ~300°C colder than that at the same depth beneath Tohoku (Model 12). From our thermal modeling, we found that the vertical temperature gradient at the continental Moho is nearly ~30°C /km and nearly 10°C /km in the slab contact zone. Therefore, if the brittle-ductile transition varies along with the depth of the interplate thermal state, the interplate thrust-type earthquakes should be deeper by ~30 km. This finding coincides with the conclusion that the down-dip part of the low-velocity structure is located at depths of 120–150 km beneath Kanto but only 80 km beneath Tohoku (Figure 6) [*Nakajima et al*., 2009b]. The low temperature and subsequent delay in dehydration at the plate interface likely account for the distribution of low seismic velocities beneath Kanto.

5.3. Distributions of Plate Water Content, Interplate Dehydration, and Seismicity Beneath Tohoku and Kanto

The down-dip limit of the hydrated upper surface of the PAC slab, with low *S*-wave velocities, reaches depths of 120–150 km beneath Kanto and is 40–70 km deeper than that beneath Tohoku [*Nakajima et al*., 2009a, 2009b]. Dehydration embrittlement has been proposed as a possible mechanism for decreasing effective normal stress and triggering intermediate-depth earthquakes [*Hasegawa et al*., 2007]. The dehydration reactions associated with the large changes in seismic velocity account for the seismicity distribution, and this relationship suggests that the phase transitions of hydrous minerals facilitate brittle failure and trigger interplate slow earthquakes. For example, the dehydration of lawsonite directly triggers earthquakes in subducting oceanic crust [*Okazaki and Hirth*, 2016].

Previous studies [*Raleigh and Paterson*, 1965; *Dobson et al*., 2002; *Omori et al*., 2004] have demonstrated a close relationship between the depth distribution of subduction zone earthquakes and dehydration reactions in intermediate (<250 km) to deep seismic zones. *Omori et al*. [2004] proposed an extended dehydration-induced earthquake hypothesis that suggests that any dehydration event has the potential to induce earthquakes in the peridotite of the subducting slab. In this study, the distributions of regional slab dehydration and seismicity at shallow depths (<150 km) beneath the Kanto-Tohoku region were similar. In this region, the basaltic oceanic crust is dehydrating under equilibrium conditions [*Hacker et al*., 2003b]. A slab consisting of gabbro, peridotite, and amphibole is generally anhydrous but is partly serpentinized by water acquired at the mid-ocean ridge [*Tucholke et al*., 1998] and outer rise [*Peacock*, 2001] and during upper slab dehydration processes [*Omori et al*., 2004]. At high temperatures and pressures, the MORB in the oceanic crust transforms from blueschist or jadeite lawsonite blueschist (<70 km) to lawsonite amphibole eclogite (70–160 km) or eclogite (>160 km). The ultramafic slab minerals transform to those of serpentinite (50 km), serpentinized chlorite dunite (80 km), chlorite-harzburgite (120–150 km), and spinel/garnet-harzburgite (150–200 km) [*Hacker et al*., 2003b].

The water content distributions in the oceanic crust and the slab interior of the PAC plate, which consist of MORB and ultramafic minerals, were calculated by using the phase diagrams of *Omori et al*. [2009] and *Hacker et al*. [2003a], respectively. The cold interplate zone on the PAC plate was composed of hydrous lawsonite blueschist with a water content of 5.4% [*Hacker et al*., 2003a, 2003b]. However, in the cold zone, a north-south trending remarkably aseismic belt was found approximately 200–300 km offshore to the east of Tohoku (Figures 7a and 7b). In this region, the dehydration of hydrous minerals does not occur due to the apparent increase in water content associated with the phase transformations from zeolite, prehnite-pumpellyite, or pumpellyite-actinolite (4.4 wt %) to lawsonite blueschist (5.4 wt %) [*Hacker et al*., 2003a] adjacent to the Japan Trench. Compared to the normal frequency of earthquakes offshore of Tohoku, substantially fewer earthquakes have occurred along this "nondehydration" belt, even if hypocentral location errors are taken into account. In contrast, to the west of the nondehydration belt, along

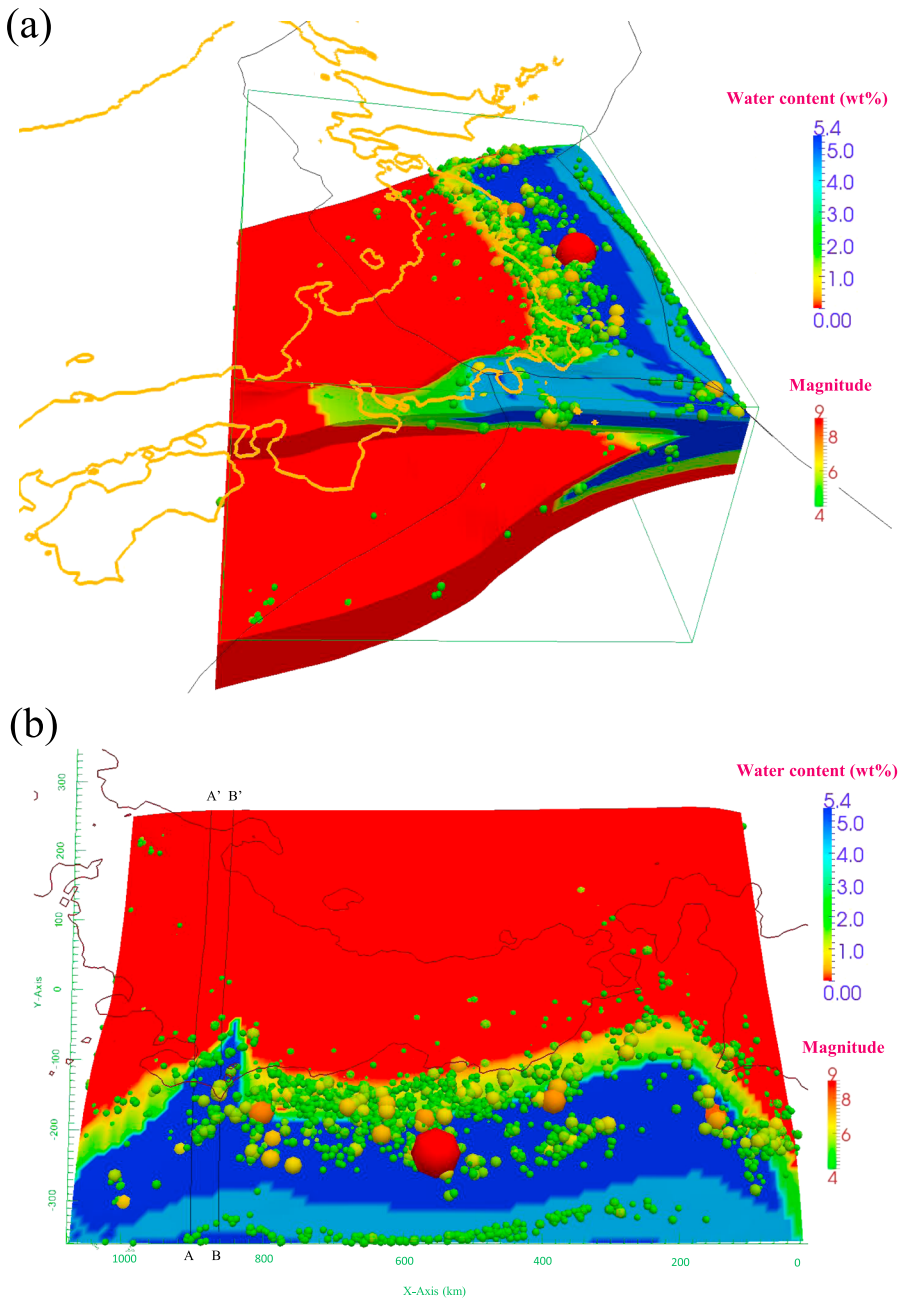

Figure 7. (a) Map view perspective of the 3-D water content distribution in the subducted PAC plate and the PHS plate beneath northeastern Japan along with the hypocenter distribution of earthquakes with magnitudes greater than 4.0 (small spheres). The hypocenters were taken from the JMA unified hypocenter data catalog (1 October 1997 to 28 February 2015). The largest red sphere represents the 2011 Tohoku-oki earthquake (*M*9.0). The color scale range of water content is 0.0 to 5.4 wt %, and the value of 5.4 wt % is the upper limit. (b) Map view perspective of the 3-D water content distribution of the upper surface of the PAC plate. Color spheres are the hypocenters of earthquakes with magnitudes greater than 4.0. Two profiles, A-A′ and B-B′, pass through the PAC-PHS slab contact zone along the upper surface of the PAC plate. The color scale range of water content is 0.0 to 5.4 wt %, and the value of 5.4 wt % is the upper limit. The portion with a value over 5.4 wt % was saturated in red.

the east coast of northeast Japan, clustered earthquakes are common in the transition zone from lawsonite blueschist (5.4 wt %), epidote blueschist (3.0 wt %), and lawsonite amphibole eclogite (3.0 wt %) to amphibole eclogite (<1.0 wt %) in the MORB of the PAC plate. More than 80% of the earthquakes (≥*M*4.0) were found to occur in this coast-parallel belt-like zone. Most earthquakes (<*M*4.0) occur along

the coast or along the Wadati-Benioff zone to depth. The phase transition of hydrous minerals was shifted to a depth of approximately 100 km, resulting in deeper hypocenters (Figures 7a and 7b).

5.4. MORB Phase Diagram, *P-T* Path, and Interplate Seismicity

According to the phase diagram of mafic rocks [*Hacker et al*., 2003a], the MORB minerals in the slab contact zone experience a longer-duration phase transition from jadeite-lawsonite-blueschist to lawsonite-amphibole-eclogite due to the low temperatures. Such hydrous mineral phase transformations increase the pore fluid pressure, reduce effective normal stress, and promote slab seismogenesis [*Kirby et al*., 1996; *Abers et al*., 2013] over a greater depth range. Old oceanic plates, such as the PAC plate beneath northeastern Japan and Alaska, are expected to exhibit greater dehydration of blueschist phases [*Abers et al*., 2013]. This relationship explains why the distribution of seismicity features a good correspondence with the isotherm in Tohoku and the anomalously cold slab contact zone beneath Kanto.

We calculated the *P-T* conditions for earthquakes located within the oceanic crust (MORB) of the subducted PAC plate (0–7 km vertically down from its upper surface) beneath Tohoku (Figure 8a) and Kanto (Figure 8b) using the unified hypocenter catalog of JMA during the period from 1 October 1997 to 28 February 2015. Earthquakes in the PAC plate at vertical distances greater than 7 km below the upper surface were not included because they are related to the phase transformations of ultramafic rock. We identified two constraints on the earthquake distribution in the MORB phase diagram [*Omori et al*., 2009] for the PAC plate. One is related to the upper left blank area ($>$3 GPa and approximately $<$600°C), which corresponds to the coldest part of the PAC plate, and the other is related to the lower right blank area ($<$1 GPa and approximately $>$300°C), which corresponds to the *P-T* constraint related to the stratified ambient temperature of the upper mantle.

In Tohoku (Figure 8a), an apparent seismic cluster exists in the depth range of 30 to 60 km (pressures of 1 to 2 GPa; dashed white ellipse) and below ~700°C, which is the transition temperature to garnet amphibolite. Most of the interplate earthquakes beneath Tohoku occurred in this region. The results in Figure 8a are consistent with the *P-T* path of interplate earthquakes in Tohoku proposed by *Hacker et al*. [2003a] and provide more detailed *P-T* conditions for the interplate seismicity in Tohoku.

In contrast, in Kanto (Figure 8b), the *P-T* conditions necessary for interplate earthquakes were shifted to the deeper depth range of 45 to 90 km (pressure of 1.5 to 3 GPa) due to the existence of a cold slab contact zone. The *P-T* conditions were estimated along profiles A-A′ and B-B′ (Figure 7b) across the slab contact zone. The profile B-B′ has a smaller PAC plate dip angle and a higher temperature than the profile A-A′. The portion that passed through the southern part (dashed red ellipse in Figure 8b) in the slab contact zone of the PAC and PHS plates has undergone more metamorphic reactions and more frequent earthquakes. The results also coincide well with the *P-T* paths beneath Kanto and Tohoku suggested by *Omori et al*. [2009]. The use of 3-D thermal convection models and the phase diagram allows us to obtain the distribution of earthquakes and related *P-T* conditions in the oceanic crust of the subducting plates (Figures 8a and 8b).

The *P-T* conditions corresponding to hypocenters were not explicitly concentrated near the phase transition boundaries, such as the transition from jadeite, lawsonite, and blueschist (5.4 wt %) to lawsonite, amphibole, and eclogite (3 wt %) or from lawsonite, amphibole, and eclogite (3 wt %) to eclogite (0 wt %). This discrepancy may be partly due to error in the determination of the geotherm and focal depths. However, if we consider the entire phase transition zone, i.e., the zone encompassing the *P-T* conditions of jadeite, lawsonite, and blueschist (5.4 wt %) to eclogite (0 wt %), most of the interplate and intraslab earthquakes ($>$70%) are located within this phase transition zone.

5.5. Relationships Among Slab Dehydration, Slow Earthquakes, and Regular Earthquakes

According to analogue experiments examining slip behavior during faulting under undrained conditions [*Chernak and Hirth*, 2011; *Hilairet et al*., 2007], the relationship between slab dehydration and regular earthquakes remains ambiguous. However, these studies also insist that slow-slip events might occur commonly under the conditions in which intermediate-depth earthquakes occur [*Chernak and Hirth*, 2011] or implicitly suggest that the viscous relaxation of serpentinite can trigger large earthquakes in subduction zones over interseismic periods of several years based on the low measured viscosity of serpentinite [*Hilairet et al*., 2007]. In addition, seismic tomography has revealed high V_p/V_s ratios and high Poisson's ratios at the base of the seismogenic zone [*Hyndman*, 2007], along with elevated pore pressures estimated from low *P*-wave velocities in the source region of very low-frequency events [*Kitajima and Saffer*, 2012]. Crack anisotropy

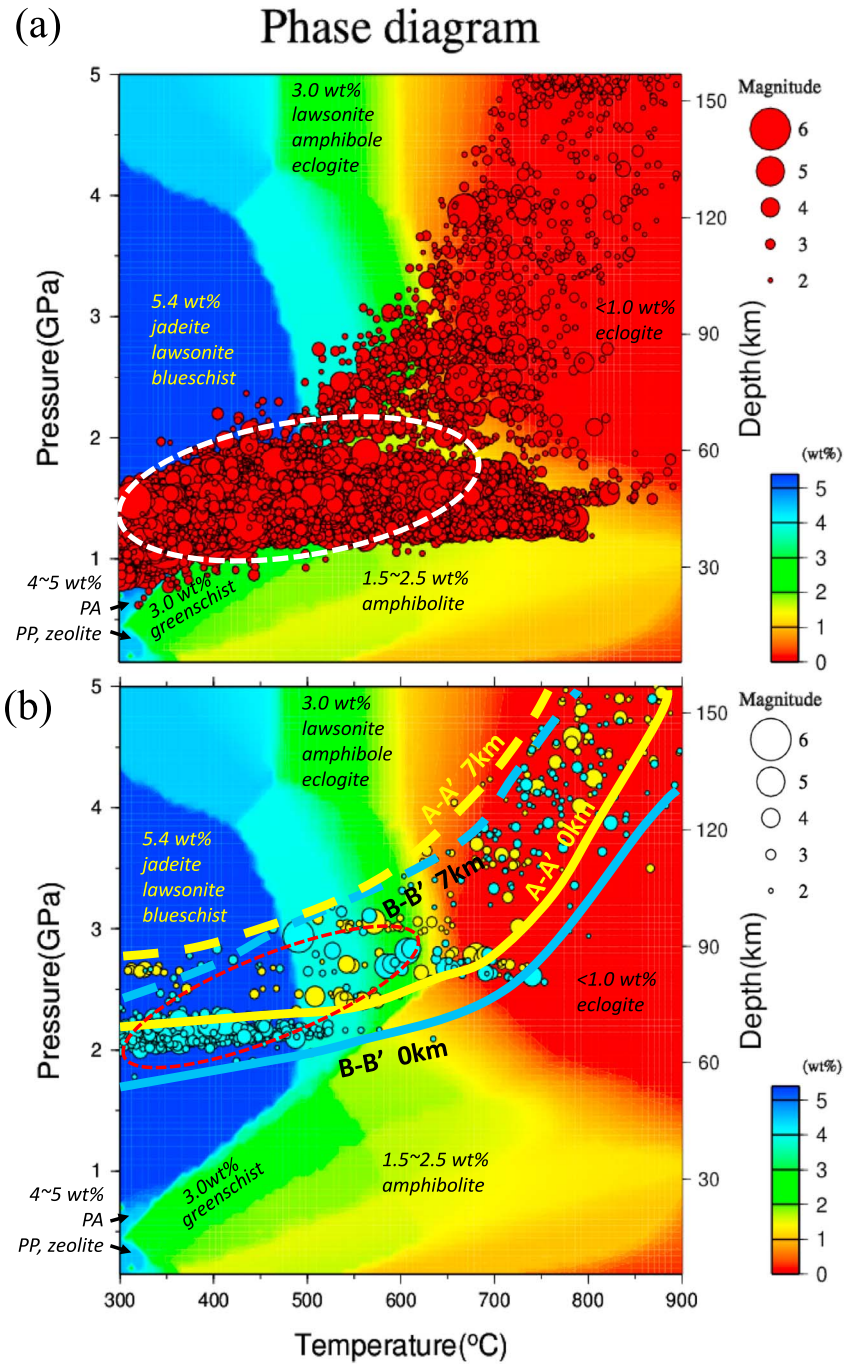

Figure 8. (a) Phase diagram for the water content of MORB in oceanic crust by *Omori et al.* [2009]. The hypocenters of earthquakes with magnitudes greater than 2.0 occurring in the oceanic crust (thickness of 7 km) of the PAC plate beneath Tohoku are also shown as solid red circles and were taken from the JMA unified hypocenter data catalog (1 October 1997 to 28 February 2015). These earthquakes were taken from the region ranging from $x = 0$ km to 800 km in Figure 7b. The area circled with the white dashed ellipse represents the depths of approximately 30 km to 60 km, where most of the interplate earthquakes beneath Tohoku are clustered. (b) Phase diagram for the water content of the MORB in the oceanic crust beneath Kanto. The hypocenters of earthquakes with a distance less than 20 km to profiles A-A′ and B-B′ in Figure 7b are also plotted. The four lines indicate the *P-T* paths for the two profiles A-A′ and B-B′ along the slab contact zone with a vertical distance of 0 km (solid lines) and 7 km (dashed lines) from the upper surface of the Pacific slab. The area circled with the red dashed ellipse represents the southern part of the slab contact zone, which has experienced more metamorphic reactions and more frequent earthquakes. Profile A-A′: the yellow solid and dashed lines denote the upper and lower surfaces of the oceanic crust, respectively. Profile B-B′: the light blue solid and dashed lines denote the upper and lower surfaces of the oceanic crust, respectively.

and high pore fluid pressure are required to produce the high V_P/V_s ratios (>2.2) recently imaged by seismic tomography in subduction zones [*Wang et al*., 2012]. Several numerical modeling studies have performed simulations of slow-slip events by using the rate- and state-dependent friction law [e.g., *Shibazaki and Shimamoto*, 2007; *Liu and Rice*, 2009; *Segall et al*., 2010]. These studies proposed that elevated pore pressure is a common requirement for emergent slow slip because a low shear stress, σ_n' [e.g., *Ikari et al*., 2013], favors stable or conditionally stable slip, and they used dilatancy hardening [*Liu*, 2013] caused by the transiently reduced pore pressure during dynamic slip nucleation to explain the faulting mechanisms of regular earthquakes. All of these factors are seemingly related to the slab dehydration-related variations in pore pressure in the subduction fault. Accordingly, the high pore fluid pressure and concomitant low fault shear stress, σ_n', not only lead to low *P*-wave velocities in the source region of slow earthquakes, such as the very low-frequency and slow-slip events, but also contribute to the high V_P/V_s ratios caused by the saturated and cracked rocks in the seismogenic zone.

Other recent studies on repeating earthquakes and small temporal changes in slow-slip rates have also demonstrated that periodic slow-slip events have triggered repeating earthquakes and megathrust earthquakes in northeastern Japan [*Kato et al*., 2012; *Ito et al*., 2013; *Uchida et al*., 2016]. Aseismic fault creep (slow slip) surrounds epicenters of repeating earthquakes and involves the rupturing of small asperities in the fault zone [*Nadeau and McEvilly*, 1999]. The rupturing process results in periodic stress perturbations at repeating intervals that usually coincide with or precede clusters of large earthquakes ($M \geq 5.0$), including the 2011 M9 Tohoku-oki earthquake. *Zhao* [2012] reported that significant structural heterogeneities have been imaged in the source areas of large earthquakes in the continental crust, subducting slab, and interplate megathrust zone. These heterogeneities represent fluids and/or magma originating from slab dehydration that can affect the rupture nucleation process of large earthquakes. *Obara and Kato* [2016] further proposed that episodic stress transfer to megathrust source faults results in an increased probability of triggering large earthquakes.

Consequently, the high pore fluid pressure caused by fluid released by slab dehydration likely not only accounts for slow earthquakes but also triggers or influences regular earthquakes along the subducted Pacific plate beneath the Kanto-Tohoku region. Consequently, the simulated thermally controlled slab dehydration zone agrees well with the interplate seismicity observed beneath the Kanto-Tohoku region.

6. Conclusions

Using 3-D numerical simulations of the complex subduction geometry beneath Japan, we have reached the following conclusions:

1. The subduction parameters tested in the generic models demonstrated that a faster or thicker oceanic plate subducting in a more trench-normal direction produces a colder slab thermal regime. The relative convergence between the two overlapping oceanic plates yields an asymmetric thermal structure in the slab contact zone.
2. A cold anomaly appears in the slab contact zone beneath Kanto, and the interplate temperature beneath offshore Kanto is approximately 300°C colder than that beneath offshore Tohoku.
3. The thermal regime and slab dehydration process control the seismicity beneath Tohoku and Kanto likely via high pore fluid pressure elevated by the slab dehydration. The spatial concurrence between variations in the thermo-dehydration state and the regional seismicity suggests that these two aspects of the subduction zone are closely related in the Kanto-Tohoku region.

Acknowledgments
We are grateful to P.J. Tackley for sharing the original 3-D source codes stag3d for our numerical simulation. We also appreciated the help of W.P. Schellart and V. Strak for their constructive comments that allowed to improve this paper. This work was partly supported by JSPS KAKENHI grant 16H04040, and the collaborative research project between Research Center for Urban Safety and Security, Kobe University, and Advanced Institute for Computational Science, Institute of Physical and Chemical Research, Japan. Some figures were created by using the Generic Mapping Tools developed by *Wessel and Smith* [1998]. We used unified hypocenter data determined by Japan Meteorological Agency. The data for this paper are available by contacting the corresponding author at jiyf@people.kobe-u.ac.jp.

References

Abers, G. A., J. Nakajima, P. E. van Keken, S. Kita, and B. R. Hacker (2013), Thermal-petrological controls on the location of earthquakes within subducting plates, *Earth Planet. Sci. Lett.*, *369*, 178–187.

Argus, D. F., R. G. Gordon, and C. DeMets (2011), Geologically current motion of 56 plates relative to the no-net-rotation reference frame, *Geochem. Geophys. Geosyst.*, *12*, Q11001, doi:10.1029/2011GC003751.

Ashi, J., H. Tokuyama, Y. Ujiie, and A. Taira (1999), Heat flow estimation from gas hydrate BSRs in the Nankai Trough: Implications for the thermal structures of the Shikoku Basin, *Eos Trans. AGU*, *80*(46), T12A-02.

Ashi, J., H. Tokuyama, and A. Taira (2002), Distribution of methane hydrate BSRs and its implication or the prism growth in the Nankai Trough, *Mar. Geol.*, *187*, 117–191.

Burkett, E. R., and M. I. Billen (2010), Three-dimensionality of slab detachment due to ridge-trench collision: Laterally simultaneous boudinage versus tear propagation, *Geochem. Geophys. Geosyst.*, *11*, Q11012, doi:10.1029/2010GC003286.

Buttles, J., and P. Olson (1998), A laboratory model of subduction zone anisotropy, *Earth Planet. Sci. Lett.*, *164*, 245–262.

Capitanio, F. A., and G. Morra (2012), The bending mechanics in a dynamic subduction system: Constraints from numerical modelling and global compilation, *Tectonophysics*, *522–523*, 224–234.

Chen, Z., W. P. Schellart, V. Strak, and J. C. Duarte (2016), Does subduction-induced mantle flow drive backarc extension?, *Earth Planet. Sci. Lett.*, *441*, 200–210, doi:10.1016/j.epsl.2016.02.027.

Chernak, L., and G. Hirth (2011), Syndeformational antigorite dehydration produces stable fault slip, *Geology*, *39*, 847–850.

Christensen, D. H., G. A. Abers, and T. L. McKnight (2003), Mantle anisotropy beneath the Alaska range inferred from S-wave splitting observations: Results from BEAAR Eos Trans. AGU, 84. Fall Meet. Suppl., Abstract S31C-0782.

Christensen, U. R. (1996), The influence of trench migration on slab penetration into the lower mantle, *Earth Planet. Sci. Lett.*, *140*, 27–39.

DeMets, C., R. G. Gordon, and D. F. Argus (2010), Geologically current plate motions, *Geophys. J. Int.*, *181*(1), 1–80, doi:10.1111/j.1365-246X.2009.04491.x.

Dobson, D. P., P. G. Meredith, and S. A. Boon (2002), Simulation of subduction zone seismicity by dehydration of serpentine, *Science*, *298*, 1407–1410.

Duarte, J. C., W. P. Schellart, and A. R. Cruden (2013), Three-dimensional dynamic laboratory models of subduction with an overriding plate and variable interplate rheology, *Geophys. J. Int.*, *195*(1), 47–66, doi:10.1093/gji/ggt257.

Enns, A., T. W. Becker, and H. Schmeling (2005), The dynamics of subduction and trench migration for viscosity stratification, *Geophys. J. Int.*, *160*, 761–775.

Faccenda, M., and F. A. Capitanio (2012), Development of mantle seismic anisotropy during subduction-induced 3-D flow, *Geophys. Res. Lett.*, *39*, L11305, doi:10.1029/2012GL051988.

Faccenda, M., and F. A. Capitanio (2013), Seismic anisotropy around subduction zones: Insights from three-dimensional modeling of upper mantle deformation and SKS splitting calculations, *Geochem. Geophys. Geosyst.*, *14*, 243–262, doi:10.1002/ggge.20055.

Funiciello, F., G. Morra, K. Regenauer-Lieb, and D. Giardini (2003), Dynamics of retreating slabs: 1. Insights from two-dimensional numerical experiments, *J. Geophys. Res.*, *108*(B4), 2206, doi:10.1029/2001JB000898.

Funiciello, F., C. Faccenna, A. Heuret, S. Lallemand, E. Di Giuseppe, and T. W. Becker (2008), Trench migration, net rotation and slab-mantle coupling, *Earth Planet. Sci. Lett.*, *271*, 233–240.

Gao, X., and K. Wang (2014), Strength of stick-slip and creeping subduction megathrusts from heat flow observations, *Science*, *345*, 1038–1041, doi:10.1126/science.1255487.

Gerya, T. (2011), Future directions in subduction modeling, *J. Geodyn.*, *5*, 344–378.

Goes, S., F. A. Capitanio, and G. Morra (2008), Evidence of lower-mantle slab penetration phases in plate motions, *Nature*, *451*, 981–984.

Grose, C. J., and J. C. Afonso (2013), Comprehensive plate models for the thermal evolution of oceanic lithosphere, *Geochem. Geophys. Geosyst.*, *14*, 3751–3778, doi:10.1002/ggge.20232.

Gurnis, M., and B. H. Hager (1988), Controls on the structure of subducted slabs, *Nature*, *335*, 317–321.

Hacker, B. R., G. A. Abers, and S. M. Peacock (2003a), Subduction factory 1. Theoretical mineralogy, densities, seismic wave speeds, and H_2O contents, *J. Geophys. Res.*, *108*(B1), 2029, doi:10.1029/2001JB001127.

Hacker, B. R., S. M. Peacock, G. A. Abers, and S. D. Holloway (2003b), Subduction factory 2. Are intermediate-depth earthquakes in subducting slabs linked to metamorphic dehydration reactions?, *J. Geophys. Res.*, *108*(B1), 2030, doi:10.1029/2001JB001129.

Hasebe, K., N. Fujii, and S. Uyeda (1970), Thermal processes under island arcs, *Tectonophysics*, *10*, 335–355.

Hasegawa, A., J. Nakajima, S. Kita, T. Okada, T. Matsuzawa, and S. H. Kirby (2007), Anomalous deepening of a belt of intraslab earthquakes in the Pacific slab crust under Kanto, central Japan: Possible anomalous thermal shielding, dehydration reactions, and seismicity caused by shallower cold slab material, *Geophys. Res. Lett.*, *34*, L09305, doi:10.1029/2007GL029616.

Hilairet, N., B. Reynard, Y. Wang, I. Daniel, S. Merkel, N. Nishiyama, and S. Petitgirard (2007), High-pressure creep of serpentine, interseismic deformation and initiation of subduction, *Science*, *318*, 1910–1913.

Hirth, G., and D. Kohlstedt (2003), Rheology of the upper mantle and the mantle wedge: A view from the experimentalists, in *Inside the Subduction Factory*, *Geophys. Monogr. Ser.*, vol. 138, edited by J. Eiler, pp. 83–105, AGU, Washington, D. C.

Honda, S. (2008), A simple semi-dynamic model of the subduction zone: Effects of a moving plate boundary on the small-scale convection under the island arc, *Geophys. J. Int.*, *173*, 1095–1105.

Honda, S., and T. Yoshida (2005), Effects of oblique subduction on the 3-D pattern of small-scale convection within the mantle wedge, *Geophys. Res. Lett.*, *32*, L13307, doi:10.1029/2005GL023106.

Hyndman, R. D. (2007), The seismogenic zone of subduction thrust faults: What we know and don't know, in *The seismogenic zone of subduction thrust faults*, edited by T. H. Dixon and J. C. Moore, Columbia Univ. Press, New York.

Ikari, M. J., C. Marone, D. M. Saffer, and A. J. Kopf (2013), Slip weakening as a mechanism for slow Earthquakes, *Nat. Geosci.*, *6*, 468–472.

Ito, Y., et al. (2013), Episodic slow slip events in the Japan subduction zone before the 2011 Tohoku-Oki earthquake, *Tectonophysics*, *600*, 14–26, doi:10.1016/j.tecto.2012.08.022.2013.

Iwamori, H. (1997), Heat sources and melting in subduction zones, *J. Geophys. Res.*, *102*, 14,803–14,820, doi:10.1029/97JB01036.

Jacoby, W. R. (1976), Paraffin model experiment of plate tectonics, *Tectonophysics*, *35*, 103–113.

Jacoby, W. R., and H. Schmeling (1982), On the effects of the lithosphere on mantle convection and evolution, *Phys. Earth Planet. Inter.*, *29*, 305–319.

Jadamec, M. A., and M. I. Billen (2010), Reconciling surface plate motions with rapid three-dimensional mantle flow around a slab edge, *Nature*, *465*, 338–341, doi:10.1038/nature09053.

Ji, Y., S. Yoshioka, and T. Matsumoto (2016), Three-dimensional numerical modeling of temperature and mantle flow fields associated with subduction of the Philippine Sea plate, southwest Japan, *J. Geophys. Res. Solid Earth*, *121*, 4458–4482, doi:10.1002/2016JB012912.

Kato, A., K. Obara, T. Igarashi, H. Tsuruoka, S. Nakagawa, and N. Hirata (2012), Propagation of slow slip leading up to the 2011 Mw 9.0 Tohoku-Oki earthquake, *Science*, *335*, 705–708.

Kimura, J., J. Robert, and T. Yoshida (2005), Reinitiation of subduction and magmatic responses in SW Japan during Neogene time, *Geol. Soc. Am. Bull.*, *117*, 969–986.

Kincaid, C., and P. Olson (1987), An experimental study of subduction and slab migration, *J. Geophys. Res.*, *92*(B13), 13,832–13,840, doi:10.1029/JB092ib13p13832.

Kirby, S. H., E. R. Engdahl, and R. Denlinger (1996), Intermediate-depth intraslab earthquakes and arc volcanism as physical expressions of crustal and uppermost mantle metamorphism in subducting slabs, in *Subduction: Top to Bottom*, *Geophys. Monogr. Ser.*, vol. 96, edited by G. E. Bebout et al., pp. 195–214, AGU, Washington, D. C.

Kita, S., T. Okada, J. Nakajima, T. Matsuzawa, and A. Hasegawa (2006), Existence of a seismic belt in the upper plane of the double seismic zone extending in the along-arc direction at depths of 70–100 km beneath NE Japan, *Geophys. Res. Lett.*, *33*, L24310, doi:10.1029/2006GL028239.

Kitajima, H., and D. M. Saffer (2012), Elevated pore pressure and anomalously low stress in regions of low frequency earthquakes along the Nankai subduction megathrust, *Geophys. Res. Lett.*, *39*, L23301, doi:10.1029/2012GL053793.
Kneller, E. A., and P. E. van Keken (2007), Trench-parallel flow and seismic anisotropy in the Mariana and Andean subduction systems, *Nature*, *450*, 1222–1226, doi:10.1038/nature06429.
Kneller, E. A., and P. E. van Keken (2008), Effect of three-dimensional slab geometry on deformation in the mantle wedge: Implications for shear wave anisotropy, *Geochem. Geophys. Geosyst.*, *9*, Q01003, doi:10.1029/2007GC001677.
Lassak, T. M., M. J. Fouch, C. E. Hall, and E. Kaminski (2006), Seismic characterization of mantle flow in subduction systems: Can we resolve a hydrated mantle wedge?, *Earth Planet. Sci. Lett.*, *243*, 632–649.
Li, Z. H., and N. M. Ribe (2012), Dynamics of free subduction from 3-D boundary element modeling, *J. Geophys. Res.*, *117*, B06408, doi:10.1029/2012JB009165.
Li, Z., Z. Xu, T. Gerya, Xu, and J. P. Burg (2013), Collision of continental corner from 3-D numerical modeling, *Earth Planet. Sci. Lett.*, *380*, 98–111.
Liu, Y. (2013), Numerical simulations on megathrust rupture stabilized under strong dilatancy strengthening in slow slip region, *Geophys. Res. Lett.*, *40*, 1311–1316, doi:10.1002/grl.50298.
Liu, Y., and J. R. Rice (2009), Slow slip predictions based on granite and gabbro friction data compared to GPS measurements in northern Cascadia, *J. Geophys. Res.*, *114*, B09407, doi:10.1029/2008JB006142.
Manea, V. C., M. Manea, V. Kostoglodov, C. A. Currie, and G. Sewell (2004), Thermal structure, coupling and metamorphism in the Mexican subduction zone beneath Guerrero, *Geophys. J. Int.*, *158*, 775–784.
Manea, V. C., M. Manea, V. Kostoglodov, and G. Sewell (2005), Thermo-mechanical model of the mantle wedge in Central Mexican subduction zone and a blob tracing approach for the magma transport, *Phys. Earth Planet. Int.*, *149*, 165–186.
Manea, V. C., M. P. Gussinyé, and M. Manea (2012), Chilean flat slab subduction controlled by overriding plate thickness, and trench rollback, *Geology*, *1*, 35–38.
Matsumoto, T. (2007), Terrestrial heat flow distribution in Japan area based on the temperature logging in the borehole of NIED Hi-net Abstract T23A-1217 paper presented at 2007 Fall Meeting, AGU, San Francisco, Calif.
McKenzie, D. P. (1967), Some remarks on heat flow and gravity anomalies, *J. Geophys. Res.*, *72*, 6261–6273, doi:10.1029/JZ072i024p06261.
McKenzie, D. P. (1968), Speculations on the consequences and causes of plate motions, *Geophys. J. R. Astron. Soc.*, *18*, 1–32.
Mishin, Y. A., T. V. Gerya, J. P. Burg, and J. A. D. Connolly (2008), Dynamics of double subduction: Numerical modeling, *Phys. Earth Planet. Inter.*, *171*, 280–295.
Morishige, M., S. Honda, and P. J. Tackley (2010), Construction of semi-dynamic model of subduction zone with given plate kinematics in 3D sphere, *Earth Planets Space*, *62*, 665–673.
Morra, G., K. Regenauer-Lieb, and D. Giardini (2006), Curvature of oceanic arcs, *Geology*, *34*, 877–880.
Morra, G., P. Chatelain, P. J. Tackley, and P. Koumoutsakos (2009), Earth curvature effects on subduction morphology: Modeling subduction in a spherical setting, *Acta Geotech.*, *4*, 95–105.
Muller, R. D., M. Sdrolias, C. Gaina, and W. R. Roest (2008), Age, spreading rates, and spreading asymmetry of the world's ocean crust, *Geochem. Geophys. Geosyst.*, *9*, Q04006, doi:10.1029/2007GC001743.
Nadeau, R. M., and T. V. McEvilly (1999), Fault slip rates at depth from recurrence intervals of repeating microearthquakes, *Science*, *285*, 718–721.
Nakajima, J. (2014), Seismic attenuation beneath Kanto, Japan: Evidence for high attenuation in the serpentinized subducting mantle, *Earth Planets Space*, *66*, 12.
Nakajima, J., and A. Hasegawa (2006), Anomalous low-velocity zone and linear alignment of seismicity along it in the subducted Pacific slab beneath Kanto, Japan: Reactivation of subducted fracture zone?, *Geophys. Res. Lett.*, *33*, L16309, doi:10.1029/2006GL026773.
Nakajima, J., and A. Hasegawa (2007), Subduction of the Philippine Sea plate beneath southwestern Japan: Slab geometry and its relationship to arc magmatism, *J. Geophys. Res.*, *112*, B08306, doi:10.1029/2006JB004770.
Nakajima, J., F. Hirose, and A. Hasegawa (2009a), Seismotectonics beneath the Tokyo metropolitan area, Japan: Effect of slab-slab contact and overlap on seismicity, *J. Geophys. Res.*, *114*, B08309, doi:10.1029/2008JB006101.
Nakajima, J., Y. Tsuji, and A. Hasegawa (2009b), Seismic evidence for thermally-controlled dehydration reaction in subducting oceanic crust, *Geophys. Res. Lett.*, *36*, L03303, doi:10.1029/2008GL036865.
Obara, K., and A. Kato (2016), Connecting slow earthquakes to huge earthquakes, *Sci. Online Ed.*, doi:10.1126/science.aaf1512.
Okazaki, K., and G. Hirth (2016), Dehydration of lawsonite could directly trigger earthquakes in subducting oceanic crust, *Nature*, *530*, 81–84.
Omori, S., T. Komabayashi, and S. Maruyama (2004), Dehydration and earthquakes in the subducting slab: Empirical link in intermediate and deep seismic zones, *Phys. Earth Planet. Inter.*, *146*, 297–311.
Omori, S., S. Kita, S. Maruyama, and M. Santosh (2009), Pressure–temperature conditions of ongoing regional metamorphism beneath the Japanese Islands, *Gondwana Res.*, *16*, 458–469.
OzBench, M., et al. (2008), A model comparison study of large-scale mantle–lithosphere dynamics driven by subduction, *Phys. Earth Planet. Inter.*, *171*, 224–234.
Peacock, S. M. (2001), Are the lower planes of double seismic zones caused by serpentine dehydration in subducting oceanic mantle?, *Geology*, *29*, 299–302.
Peacock, S. M., and K. Wang (1999), Seismic consequences of warm versus cool subduction metamorphism, examples from Southwest and Northeast Japan, *Science*, *286*, 937–939.
Peacock, S. M., P. E. van Keken, S. D. Holloway, B. R. Hacker, G. Abers, and R. L. Fergason (2005), Thermal structure of the Costa Rica-Nicaragua subduction zone: Slab metamorphism, seismicity and arc magmatism, *Phys. Earth Planet. Inter.*, *149*, 187–200.
Pollack, H. N., S. J. Hurter, and J. R. Johnson (1993), Heat flow from the Earth 's interior: Analysis of the global data set, *Rev. Geophys.*, *31*(3), 267–280, doi:10.1029/93RG01249.
Raleigh, C. B., and M. S. Paterson (1965), Experimental deformation of serpentinite and its tectonic implications, *J. Geophys. Res.*, *70*, 3965–3985, doi:10.1029/JZ070i016p03965.
Ranalli, G. (1995), *Rheology of the Earth*, 2nd ed., pp. 76, Chapman and Hall, London.
Ribe, N. M. (2010), Bending mechanics and mode selection in free subduction: A thin-sheet analysis, *Geophys. J. Int.*, *180*, 559–576.
Russo, R. M., and P. G. Silver (1994), Trench-parallel flow beneath the Nazca plate from seismic anisotropy, *Science*, *263*, 1105–1111.
Schellart, W. P. (2004), Kinematics of subduction and subduction-induced flow in the upper mantle, *J. Geophys. Res.*, *109*, B07401, doi:10.1029/2004JB002970.
Schellart, W. P., and L. Moresi (2013), A new driving mechanism for backarc extension and backarc shortening through slab sinking induced toroidal and poloidal mantle flow: Results from dynamic subduction models with an overriding plate, *J. Geophys. Res. Solid Earth*, *118*, 3221–3248, doi:10.1002/jgrb.50173.

Schellart, W. P., J. Freeman, D. R. Stegman, L. Moresi, and D. May (2007), Evolution and diversity of subduction zones controlled by slab width, *Nature*, *446*, 308–311, doi:10.1038/nature05615.
Schmeling, H., et al. (2008), A benchmark comparison of spontaneous subduction models—Towards a free surface, *Phys. Earth Planet. Inter.*, *171*, 198–223.
Sdrolias, M. R., and D. Muller (2006), Controls on back-arc basin formation, *Geochem. Geophys. Geosyst.*, *7*, Q04016, doi:10.1029/2005GC001090.
Segall, P., A. M. Rubin, A. M. Bradley, and J. R. Rice (2010), Dilatant strengthening as a mechanism for slow slip events, *J. Geophys. Res.*, *115*, B12305, doi:10.1029/2010JB007449.
Shibazaki, B., and T. Shimamoto (2007), Modeling of short-interval silent slip events in deeper subduction zone interfaces considering the frictional properties at the unstable_stable transition regime, *Geophys. J. Int.*, *171*, 191–205.
Sleep, N., and M. N. Toksöv (1971), Evolution of marginal basins, *Nature*, *233*, 548–550.
Smith, G. P., D. A. Wiens, K. M. Fischer, L. M. Dorman, S. C. Webb, and J. A. Hildebrand (2001), A complex pattern of mantle flow in the Lau backarc, *Science*, *292*, 713–716, doi:10.1126/science.1058763.
Stegman, D. R., J. Freeman, W. P. Schellart, L. Moresi, and D. May (2006), Influence of trench width on subduction hinge retreat rates in 3-D models of slab rollback, *Geochem. Geophys. Geosyst.*, *7*, Q03012, doi:10.1029/2005GC001056.
Stegman, D. R., R. Farrington, F. A. Capitanio, and W. P. Schellart (2010a), A regime diagram for subduction styles from 3-D numerical models of free subduction, *Tectonophysics*, *483*, 29–45.
Stegman, D. R., W. P. Schellart, and J. Freeman (2010b), Competing influences of plate width and far-field boundary conditions on trench migration and morphology of subducted slabs in the upper mantle, *Tectonophysics*, *483*, 46–57.
Stein, C. A., and S. Stein (1992), A model for the global variation in oceanic depth and heat flow with lithospheric age, *Nature*, *359*, 123–129.
Strak, V., and W. P. Schellart (2014), Evolution of 3-D subduction-induced mantle flow around lateral slab edges in analogue models of free subduction analyzed by stereoscopic particle image velocimetry technique, *Earth Planet. Sci. Lett.*, *403*, 368–379.
Strak, V., and W. P. Schellart (2016), Control of slab width on subduction-induced upper mantle flow and associated upwellings: Insights from analog models, *J. Geophys. Res. Solid Earth*, *121*, 4641–4654, doi:10.1002/2015JB012545.
Tackley, P. J. (1998), Self-consistent generation of tectonic plates in three-dimensional mantle convection, *Earth Planet. Sci. Lett.*, *157*, 9–22.
Tackley, P. J., and S. Xie (2003), Stag3D: A code for modeling thermo-chemical multiphase convection in Earth's mantle, in *Computational Fluid and Solid Mechanics 2003*, edited by K. J. Bathe, pp. 1524–1527, Elsevier, Amsterdam.
Takahashi, M. (2006), Tectonic development of the Japanese islands controlled by the Philippine Sea plate motion, *J. Geogr.*, *115*, 116–123.
Tanaka, A., M. Yamano, Y. Yano, and M. Sasada (2004), Geothermal gradient and heat flow data in and around Japan, digital geoscience map, DGMP-5, *Geol. Surv. Jpn*.
Tucholke, B. E., J. Lin, and M. C. Kleinrock (1998), Megamullions and mullion structure defining oceanic metamorphic core complexes on the MidAtlantic Ridge, *J. Geophys. Res.*, *103*, 9857–9866, doi:10.1029/98JB00167.
Turcotte, D. L., and G. Schubert (2002), *Geodynamics*, 2nd ed., pp. 186, Cambridge Univ. Press, Cambridge, U. K.
Uchida, N., T. Matsuzawa, J. Nakajima, and A. Hasegawa (2010), Subduction of a wedge-shaped Philippine Sea plate beneath Kanto, central Japan, estimated from converted waves and small repeating earthquakes, *J. Geophys. Res.*, *115*, B07309, doi:10.1029/2009JB006962.
Uchida, N., T. Iinuma, R. M. Nadeau, R. Bürgmann, and R. Hino (2016), Periodic slow slip triggers megathrust zone earthquakes in northeastern Japan, *Science*, *351*, 488, doi:10.1126/science.aad3108.
van Keken, P. E. (2003), The structure and dynamics of the mantle wedge, *Earth Planet. Sci. Lett.*, *215*, 323–338.
van Keken, P. E., et al. (2008), A community benchmark for subduction zone modeling, *Phys. Earth Planet. Inter.*, *171*, 187–197.
van Keken, P. E., B. R. Hacker, E. M. Syracuse, and G. A. Abers (2011), Subduction factory: 4. Depth-dependent flux of H_2O from subducting slabs worldwide, *J. Geophys. Res.*, *116*, B01401, doi:10.1029/2010JB007922.
Wada, I., and K. Wang (2009), Common depth of slab-mantle decoupling: Reconciling diversity and uniformity of subduction zones, *Geochem. Geophys. Geosyst.*, *10*, Q10009, doi:10.1029/2009GC002570.
Wada, I., and S. King (2015), Dynamics of subducting slabs: Numerical modeling and constraints from seismology, geoid topography, geochemistry, and petrology, in *Treatise of Geophysics*, 2nd ed., vol. 7, edited by G. Schubert, pp. 339–391, Elsevier, Amsterdam.
Wada, I., K. Wang, J. He, and R. D. Hyndman (2008), Weakening of the subduction interface and its effects on surface heat flow, slab dehydration, and mantle wedge serpentinization, *J. Geophys. Res.*, *113*, B04402, doi:10.1029/2007JB005190.
Wada, I., J. He, A. Hasegawa, and J. Nakajima (2015), Mantle wedge flow pattern and thermal structure in Northeast Japan: Effects of oblique subduction and 3-D slab geometry, *Earth Planet. Sci. Lett.*, *426*, 76–88, doi:10.1016/j.epsl.2015.06.021.
Wang, K., R. D. Hyndman, and M. Yamano (1995), Thermal regime of the southwest Japan subduction zone: Effects of age history of the subducting plate, *Tectonophysics*, *248*, 53–69.
Wang, K., I. Wada, and Y. Ishikawa (2004), Stresses in the subducting slab beneath southwest Japan and relation with plate geometry, tectonic forces, slab dehydration, and damaging earthquakes, *J. Geophys. Res.*, *109*, B08304, doi:10.1029/2003JB002888.
Wang, X. Q., A. Schubnel, J. Fortin, E. C. David, Y. Guéguen, and H. K. Ge (2012), High Vp/Vs ratio: Saturated cracks or anisotropy effects? *Geophys. Res. Lett.*, *39*, L11307, doi:10.1029/2012GL051742.
Wessel, P., and W. H. F. Smith (1998), New, improved version of the generic mapping tools released, *Eos Trans. AGU*, *79*, 579, doi:10.1029/98EO00426.
Yamano, M. (2004), Heat flow data in and around Japan, Digital Geoscience Map DGM P-5 Geological Survey of Japan.
Yamasaki, T., and T. Seno (2003), Double seismic zone and dehydration embrittlement of the subducting slab, *J. Geophys. Res.*, *108*(B4), 2212, doi:10.1029/2002JB001918.
Yoshida, M., F. Tajima, S. Honda, and M. Morishige (2012), The 3D numerical modeling of subduction dynamics: Plate stagnation and segmentation, and crustal advection in the wet mantle transition zone, *J. Geophys. Res.*, *117*, B04104, doi:10.1029/2011JB008989.
Yoshii, T. (1975), Regionality of group velocities of Rayleigh waves in the Pacific and thickening of the plate, *Earth Planet. Sci. Lett.*, *25*, 305–312.
Yoshioka, S., and K. Murakami (2007), Temperature distribution of the upper surface of the subducted Philippine Sea plate, southwest Japan, from a three-dimensional subduction model: Relation to large interplate and low-frequency earthquakes, *Geophys. J. Int.*, *171*, 302–315.
Yoshioka, S., M. Toda, and J. Nakajima (2008), Regionality of deep low frequency earthquakes associated with subduction of the Philippine Sea plate along the Nankai Trough, southwest Japan, *Earth Planet. Sci. Lett.*, *272*, 189–198.

Yoshioka, S., Y. Suminokura, T. Matsumoto, and J. Nakajima (2013), Two-dimensional thermal modeling of subduction of the Philippine Sea plate beneath southwest Japan, *Tectonophysics*, *608*, 1094–1108.

Yoshioka, S., R. Takagi, and T. Matsumoto (2015), Relationship between temperatures and fault slips on the upper surface of the subducting Philippine Sea Plate beneath Kanto district, central Japan, *Geophys. J. Int.*, *201*, 878–890.

Zhao, D. (2012), Tomography and dynamics of Western-Pacific subduction zones, *Monogr. Environ. Earth Planets*, *1*, 1–70, doi:10.5047/meep.2012.00101.0001.

Zhu, G., Y. Shi, and P. Tackley (2010), Subduction of the western Pacific plate underneath northeast China: Implications of numerical studies, *Phys. Earth Planet. Inter.*, *178*, 92–99.